



OPEN Efficient elimination of basic red 9 from wastewater using ceramic metal oxides containing carbon as novel nanohybrids

Nada S. Al-Kadhi¹, Saad A. Aljlil², Maram T. Basha³ & Ehab A. Abdelrahman⁴✉

Basic red 9 is a cationic triphenylmethane dye of considerable environmental concern because of its toxicity, persistence, and harmful impact on aquatic systems. In this study, two multiphase ceramic metal oxide/carbon nanohybrids, namely $\text{Sr}_6\text{Co}_5\text{O}_{14.3}/\text{SrCO}_3/\text{MgO}/\text{C}$ (MSC600) and $\text{SrCoO}_{2.5}/\text{SrCO}_3/\text{MgO}/\text{Sr}(\text{OH})_2 \cdot \text{H}_2\text{O}/\text{C}$ (MSC800), were synthesized via the Pechini sol-gel method at 600 and 800 °C, respectively. The synthesized nanohybrids were evaluated for the adsorption of basic red 9 from wastewater. XRD confirmed the multiphase crystalline structures of both nanohybrids, with average crystallite sizes of 58.12 nm for MSC600 and 68.62 nm for MSC800. EDX verified the presence of Mg, O, C, Co, and Sr in both samples, while FE-SEM and HR-TEM revealed marked morphology evolution from a more open rod-like network in MSC600 to more compact spherical/polyhedral aggregates in MSC800. Adsorption experiments demonstrated superior maximum capacities of 436.68 mg/g for MSC600 and 313.48 mg/g for MSC800. The adsorption process was found to be physical, spontaneous, exothermic, and followed the Langmuir isotherm and pseudo-first-order kinetic model. Both nanohybrids also exhibited good regeneration/reuse behavior and maintained high removal efficiency in real laboratory wastewater. These findings highlight the strong potential of the developed multiphase nanohybrids for the efficient treatment of basic red 9-contaminated wastewater.

Keywords Basic red 9 dye, Pechini sol gel synthesis, Nanohybrid, Adsorption kinetics and isotherms, Wastewater treatment

Rapid industrialization and urban expansion have substantially increased the discharge of colored effluents into natural water bodies, mainly due to the extensive use of synthetic organic dyes in textiles, leather, paper, plastics, cosmetics, food products, and routine laboratory activities^{1–3}. In many industrial applications, only a small proportion of the applied dye is retained on the product, whereas the remainder is lost with process water, leading to the continuous generation of highly colored effluents that may be discharged with insufficient treatment^{4–6}. Because synthetic dyes typically possess stable aromatic frameworks and resistant functional groups, they persist in aquatic systems and, even at low concentrations, can hinder light penetration, inhibit photosynthesis, reduce oxygen levels, and disturb the equilibrium of aquatic ecosystems^{7,8}. Many dyes, together with their degradation products, may possess toxic, mutagenic, or carcinogenic properties, and long-term exposure through contaminated water, irrigation pathways, or fish consumption may therefore result in serious adverse health effects^{9,10}. Moreover, their tendency to associate with sediments and soil matrices favors persistent environmental accumulation and progressive groundwater contamination, which renders remediation both complex and expensive, particularly in arid areas reliant on aquifers as major water resources^{11,12}. Basic red 9 is a cationic triphenylmethane dye widely employed in textile, paper, and laboratory applications, and its presence in wastewater is especially concerning because of its toxicological relevance, strong interaction with biological macromolecules, and detrimental impact on aquatic life¹³. Several techniques have been investigated for the treatment of dye-contaminated water, most notably membrane filtration^{14–16}, coagulation/flocculation^{17,18}, electrodialysis¹⁹, photocatalytic degradation^{20,21}, bioremediation^{22,23}, and adsorption^{24,25}. Nevertheless, membrane processes are often limited by fouling and concentrate management, coagulation/flocculation leads

¹Department of Chemistry, College of Science, Princess Nourah bint Abdulrahman University, P.O. Box 84428, Riyadh 11671, Saudi Arabia. ²Water Management and Treatment Technologies Institute, King Abdulaziz City for Science and Technology, P.O. Box 6086, Riyadh 11442, Saudi Arabia. ³Department of Chemistry, College of Science, University of Jeddah, Jeddah 21589, Saudi Arabia. ⁴Department of Chemistry, College of Science, Imam Mohammad Ibn Saud Islamic University (IMSIU), Riyadh 11623, Saudi Arabia. ✉email: EAAAhmed@imamu.edu.sa

to considerable sludge production, electro dialysis is constrained by technical complexity and energy demand, photocatalytic degradation may be less effective in real systems, and bioremediation generally requires carefully controlled conditions and remains vulnerable to inhibitory wastewater components. By comparison, adsorption has gained particular importance because it combines high dye removal efficiency with operational simplicity, flexibility, ease of regeneration, no requirement for sophisticated equipment, and strong potential for practical scale-up. Metal oxide nanoparticles are promising adsorbents for dye-laden water owing to their structural stability, surface reactivity, and the ease with which their composition and morphology can be tailored to favor interactions with ionic dye molecules^{26–30}. When combined with carbonaceous phases^{31–36} or multiple oxide constituents^{37–41}, they can form hybrid materials with a broader range of active sites and improved adsorption efficiency, particularly in complex real wastewater systems containing competing species. The Pechini sol-gel method is widely regarded as a versatile route for the preparation of multicomponent metal oxide nanoparticles, chiefly because it ensures molecular-level mixing of metal ions and allows precise control over composition and stoichiometry^{42–47}. Moreover, the decomposition of the polymeric precursor can facilitate the formation of nanostructured oxide or oxide/carbon materials at relatively low calcination temperatures, with favorable control over microstructure and porosity^{48–56}. Only a few adsorbents have been examined for basic red 9 removal, including activated carbon (69.82 mg/g)⁵⁷, lignocellulosic materials (48.98 mg/g)⁵⁸, biochar (52.30 mg/g)⁵⁹, and rice husk (7.20 mg/g)⁶⁰. Previously reported adsorbents for basic red 9 generally show limited adsorption capacities and insufficient validation in terms of regeneration, tolerance to competing ions, and performance in real wastewater. Meanwhile, multiphase ceramic metal oxide/carbon nanohybrids derived from the Pechini sol-gel route remain largely unexplored for this application. Accordingly, the novelty of the present work lies in the development of two new Sr-Co-Mg-based multiphase ceramic metal oxide/carbon nanohybrids, MSC600 ($\text{Sr}_6\text{Co}_5\text{O}_{14.3}/\text{SrCO}_3/\text{MgO}/\text{C}$) and MSC800 ($\text{SrCoO}_{2.5}/\text{SrCO}_3/\text{MgO}/\text{Sr}(\text{OH})_2\cdot\text{H}_2\text{O}/\text{C}$), synthesized by the Pechini sol-gel method at 600 and 800 °C, respectively, for the efficient removal of basic red 9 dye from wastewater. The consideration of multiple phases is particularly important in the present work because a single-phase adsorbent often provides only a limited type and density of active sites, whereas a multiphase ceramic oxide/carbon system can offer chemically diverse surface domains and complementary adsorption functions. This synthesis strategy enabled the coexistence of multiple ceramic oxide phases and a carbonaceous component within a single material, which can enhance electrostatic interactions, hydrogen bonding, π - π interaction, and surface complexation with the cationic dye. In addition, the work advances current research by linking phase composition and morphology to adsorption performance and by demonstrating high capacity, favorable kinetics, spontaneous and exothermic behavior, regeneration/reuse capability, and effective treatment of both synthetic and real laboratory wastewater. The environmental relevance of the present work also aligns with Sustainable Development Goal 6 (SDG 6), which aims to ensure the availability and sustainable management of water and sanitation for all. In particular, SDG 6 emphasizes improving water quality by reducing pollution and enhancing wastewater treatment^{61–64}. From this perspective, the development of efficient adsorbent nanohybrids for the removal of hazardous dyes from contaminated water is not only scientifically important, but also directly related to global sustainability efforts directed toward cleaner and safer water resources.

Materials and methods

Materials

The chemicals used in this study were tartaric acid ($\text{C}_4\text{H}_6\text{O}_6$), cobalt nitrate hexahydrate ($\text{Co}(\text{NO}_3)_2\cdot 6\text{H}_2\text{O}$), sodium hydroxide (NaOH), polyethylene glycol 400 ($\text{H}(\text{OCH}_2\text{CH}_2)_n\text{OH}$), hydrochloric acid (HCl), magnesium nitrate hexahydrate ($\text{Mg}(\text{NO}_3)_2\cdot 6\text{H}_2\text{O}$), potassium chloride (KCl), strontium nitrate ($\text{Sr}(\text{NO}_3)_2$), and basic red 9 dye ($\text{C}_{19}\text{H}_{18}\text{N}_3\text{Cl}$). All chemicals were of high purity and were obtained from Sigma Aldrich and used without further purification. Distilled water was used throughout all synthesis procedures and for the preparation of dye and reagent solutions.

Synthesis of $\text{Sr}_6\text{Co}_5\text{O}_{14.3}/\text{SrCO}_3/\text{MgO}/\text{C}$ and $\text{SrCoO}_{2.5}/\text{SrCO}_3/\text{MgO}/\text{Sr}(\text{OH})_2\cdot\text{H}_2\text{O}/\text{C}$ nanohybrids

$\text{Sr}_6\text{Co}_5\text{O}_{14.3}/\text{SrCO}_3/\text{MgO}/\text{C}$ and $\text{SrCoO}_{2.5}/\text{SrCO}_3/\text{MgO}/\text{Sr}(\text{OH})_2\cdot\text{H}_2\text{O}/\text{C}$ nanocomposites were synthesized by the Pechini sol-gel technique as illustrated in Fig. 1. In this method, 35 g of tartaric acid was solubilized in about 100 mL of distilled water. Also, a mixed metal ion solution containing 20 g of $\text{Mg}(\text{NO}_3)_2\cdot 6\text{H}_2\text{O}$, 20 g of $\text{Sr}(\text{NO}_3)_2$, as well as 20 g of $\text{Co}(\text{NO}_3)_2\cdot 6\text{H}_2\text{O}$ was prepared using 200 mL of distilled water. The tartaric acid chelating solution was slowly added to the mixed nitrate solution under continuous agitation, then 15 mL of polyethylene glycol 400 were added, and the blend was heated at 200 °C till the solvent completely evaporated and a dry precursor gel was obtained. The dried precursor was gently ground and calcined in air at 600 °C for 3 h to yield the $\text{Sr}_6\text{Co}_5\text{O}_{14.3}/\text{SrCO}_3/\text{MgO}/\text{C}$ nanohybrid denoted MSC600 and at 800 °C for 3 h to yield the $\text{SrCoO}_{2.5}/\text{SrCO}_3/\text{MgO}/\text{Sr}(\text{OH})_2\cdot\text{H}_2\text{O}/\text{C}$ nanohybrid denoted MSC800.

The selection of 600 and 800 °C in the present work was scientifically based on the thermal evolution behavior of the investigated Sr-Co-Mg-based precursor system. At temperatures below 600 °C, the obtained product remained predominantly amorphous, whereas calcination at 600 °C led to the formation of a crystalline nanohybrid with a defined phase composition (MSC600), indicating that this temperature is critical for the development of the desired crystalline structure. A higher calcination temperature of 800 °C was then employed to further examine the thermal evolution of the material, resulting in the formation of another crystalline nanohybrid with different components (MSC800) and structural characteristics. Accordingly, MSC600 and MSC800 nanohybrids were comparatively investigated in terms of crystallite size, surface area, morphology, and adsorption performance toward basic red 9 dye, thereby establishing the temperature-dependent structure-property relationship of this newly developed system.

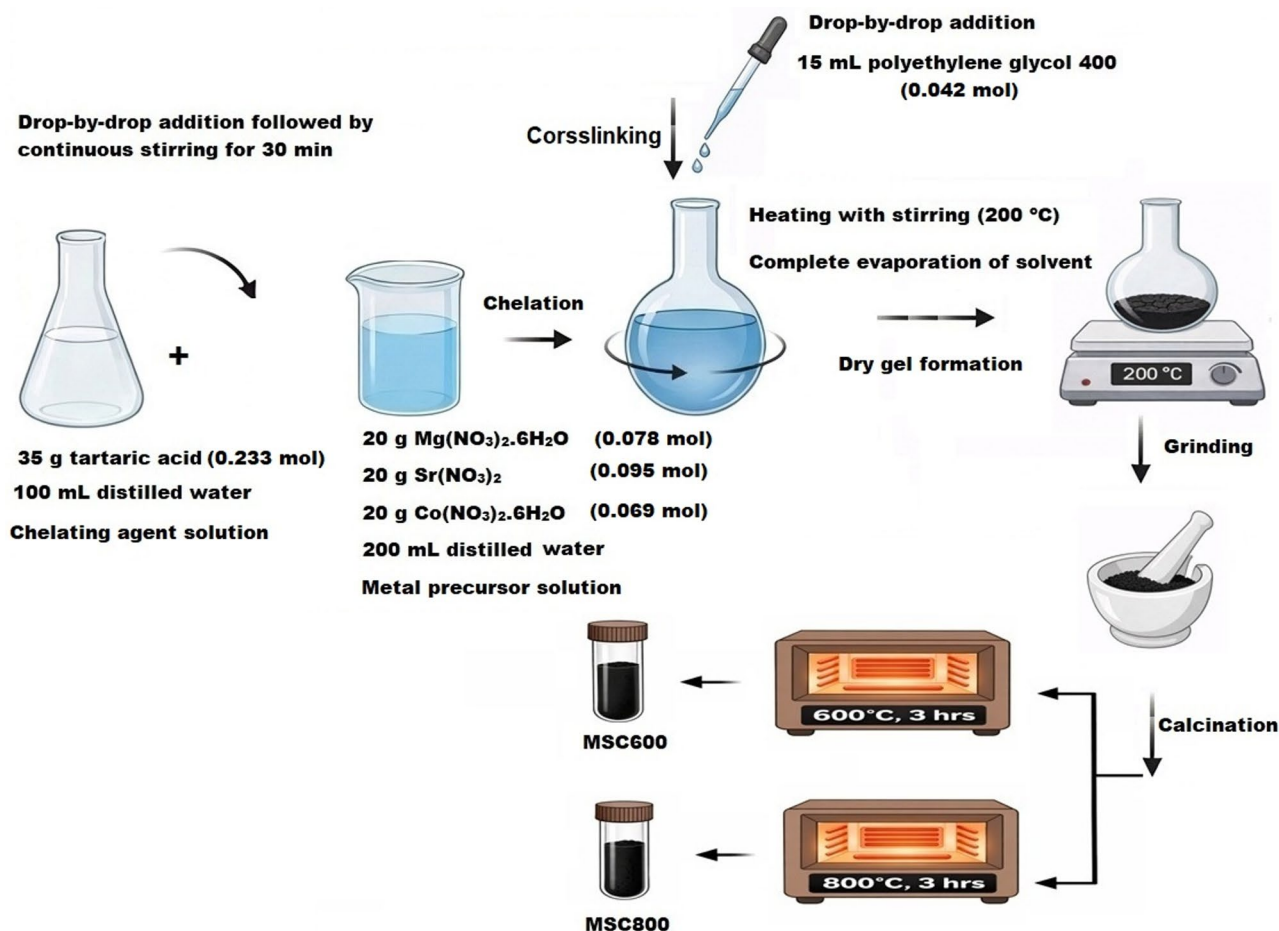


Fig. 1. Schematic diagram of the Pechini sol gel process employed for the production of $\text{Sr}_6\text{Co}_5\text{O}_{14.3}/\text{SrCO}_3/\text{MgO}/\text{C}$ and $\text{SrCoO}_{2.5}/\text{SrCO}_3/\text{MgO}/\text{Sr}(\text{OH})_2 \cdot \text{H}_2\text{O}/\text{C}$ nanohybrids.

Instrumentation

The crystal structure of all constructed nanohybrids was examined employing an X-ray diffraction diffractometer (D8 Discover, Bruker, USA). The morphology as well as surface elemental composition were investigated by a field emission scanning electron microscope outfitted with energy dispersive X-ray spectroscopy (FE-SEM/EDX Quanta 250 FEG, Thermo Fisher Scientific, USA). Fourier transform infrared (FT-IR) spectra were recorded using a Nicolet spectrometer in the range of 400–4000 cm^{-1} employing the KBr pellet technique to identify surface functional groups and monitor changes after dye adsorption. N_2 adsorption/desorption measurements were performed at 77 K employing a NOVAtouch surface area and pore size analyzer (Quantachrome, USA) after degassing the samples at 150 °C for 4 h to determine the total pore volume, BET surface area, and mean pore diameter of the samples. The detailed nanoscale characteristics were studied by a high-resolution transmission electron microscope (HR-TEM JEM 2100Plus, JEOL Ltd., Japan). The concentration of basic red 9 dye in solution during adsorption experiments was estimated employing a UV-Vis spectrophotometer (Cintra 3030, GBC, Australia).

Adsorption of basic red 9 dye pollutant from aqueous solutions

Batch adsorption experiments were performed to remove basic red 9 dye from aqueous solutions using the synthesized nanocomposites under the conditions listed in Table 1, and all dye suspensions were continuously stirred on a magnetic stirrer during the tests. After each experiment, the solid nanocomposite was separated from the liquid phase using a centrifuge, and the concentration of basic red 9 dye in the filtrate was determined with a UV-Vis spectrophotometer at 545 nm. The removal percentage of basic red 9 dye (% R) was calculated using Eq. (1). The adsorption capacity of the nanocomposite (Q , mg/g) was obtained from Eq. (2)^{65–68}.

$$\%R = \frac{C_o - C_e}{C_o} \times 100 \quad (1)$$

$$Q = (C_o - C_e) \times \frac{V}{W} \quad (2)$$

Influence	Studied conditions					
	V (mL)	C _o (mg/L)	T (K)	W (g)	t (min)	pH
pH	150	300	298	0.1	300	2–10
Contact time	150	300	298	0.1	10–100	10
Solution temperature	150	300	298–328	0.1	60 (MSC600) 80 (MSC800)	10
Concentration of basic red 9 dye	150	100–400	298	0.1	60 (MSC600) 80 (MSC800)	10

Table 1. Experimental parameters affecting the removal of basic red 9 using synthesized nanohybrids.

In these equations, C_o and C_e are the initial and equilibrium dye concentrations in mg/L, V is the solution volume in L, and W is the mass of adsorbent in g.

To ensure reproducibility, all adsorption experiments were conducted in triplicate under identical experimental conditions using independently prepared samples for each run. The data presented in the corresponding figures were plotted as the mean values of the three measurements, while the error bars represent the standard deviation of these measurements.

Regeneration of the basic red 9 laden adsorbent was performed by contacting exhausted nanocomposite with 100 mL of hydrochloric acid solutions at concentrations of 1 M, 1.5 M, and 2 M for 60 min, followed by separation of the solid phase and spectrophotometric determination of the dye content in the eluate. The desorption percentage of basic red 9 dye, denoted as % D, was calculated using Eq. (3)^{69–72}.

$$\%D = \frac{100C_dV_d}{(C_o - C_e)V} \quad (3)$$

In this equation, C_d represents the basic red 9 dye concentration in the desorption solution in mg/L, and V_d is the volume of the desorption solution in L.

Reusability of the products was assessed over five successive cycles by contacting 0.1 g of adsorbent with 150 mL of basic red 9 solution at an initial concentration of 300 mg/L at 298 K and pH 10 for 60 min for MSC600 and 80 min for MSC800 under continuous stirring. After each cycle the dye-loaded adsorbent was separated, regenerated with 100 mL of 2 M hydrochloric acid, washed with distilled water, and subsequently applied again under identical conditions, and the residual basic red 9 concentration was measured after each run to evaluate the robustness of the adsorption performance.

Binary adsorption tests were performed to investigate how coexisting ions influence the elimination of basic red 9 onto MSC600 and MSC800 nanocomposites. All tests were implemented at pH 10 as well as 298 K with a preliminary basic red 9 concentration of 300 mg/L, keeping the molar ratio of basic red 9 to each competing ion equal to 1:1. The competing species comprised K⁺, Na⁺, Ca²⁺, Mg²⁺, NO₃⁻, Cl⁻, crystal violet, and methylene blue, which are typical cationic and anionic components present in aqueous systems. Batch adsorption tests were carried out by introducing 0.1 g of each nanohybrid into 150 mL of dye solution comprising the respective coexisting ion. The suspensions were agitated for 60 min concerning MSC600 as well as 80 min concerning MSC800 to ensure equilibrium conditions. After contact, the residual basic red 9 concentration was estimated employing a UV–Vis spectrophotometer, then the uptake capabilities were calculated from mass balance considerations.

pH_{PZC} of nanohybrids

The point of zero charge (pH_{PZC}) of MSC600 and MSC800 nanohybrids was identified by a batch approach in which 0.1 g of nanocomposite was added to 50 mL of 0.01 M KCl solution adjusted to different initial pH values (pH_I) using dilute HCl or NaOH, and the dispersions were agitated at room temperature until equilibrium, and the final pH (pH_F) was then recorded. For each suspension the pH shift, ΔpH, was evaluated based on Eq. (4). pH_{PZC} for each nanocomposite was obtained from the plot of ΔpH versus pH_I as the pH value at which ΔpH becomes zero^{73–76}.

$$\Delta\text{pH} = \text{pH}_F - \text{pH}_I \quad (4)$$

Results and discussion

Characterization results

XRD

According to the diffraction patterns shown in Fig. 2A, the MSC600 nanocomposite consists of rhombohedral Sr₆Co₅O_{14.3} identified by card JCPDS 01 079 6139, orthorhombic SrCO₃ identified by card JCPDS 00 005 0418, and cubic MgO identified by card JCPDS 01 087 0653. The reflections of the rhombohedral Sr₆Co₅O_{14.3} phase appear at 2θ values of 18.89, 28.28, 32.69, 38.62, 46.64, 47.74, 55.59, 57.27, 59.61, 63.88, 65.27, 66.65, 68.57, 75.06, 75.89, and 77.55, which correspond to the (110), (1 1–3), (300), (220), (2 1–5), (1 1–6), (036), (2 3–4), (1 2–7), (511), (5 1–2), (3 1–7), (505), (155), (3 3–6), and (3 4–4) planes, respectively. The orthorhombic SrCO₃ phase in MSC600 shows characteristic peaks at 2θ values of 20.28, 21.09, 25.24, 25.79, 29.66, 31.32, 34.48, 35.17, 36.56, 39.72, 41.39, 44.15, 45.66, 49.94, 51.59, 52.98, 55.04, 58.92, 72.02, and 73.69, which are indexed to the (110), (020), (111), (021), (002), (121), (102), (200), (130), (211), (220), (221), (041), (113), (222), (042),

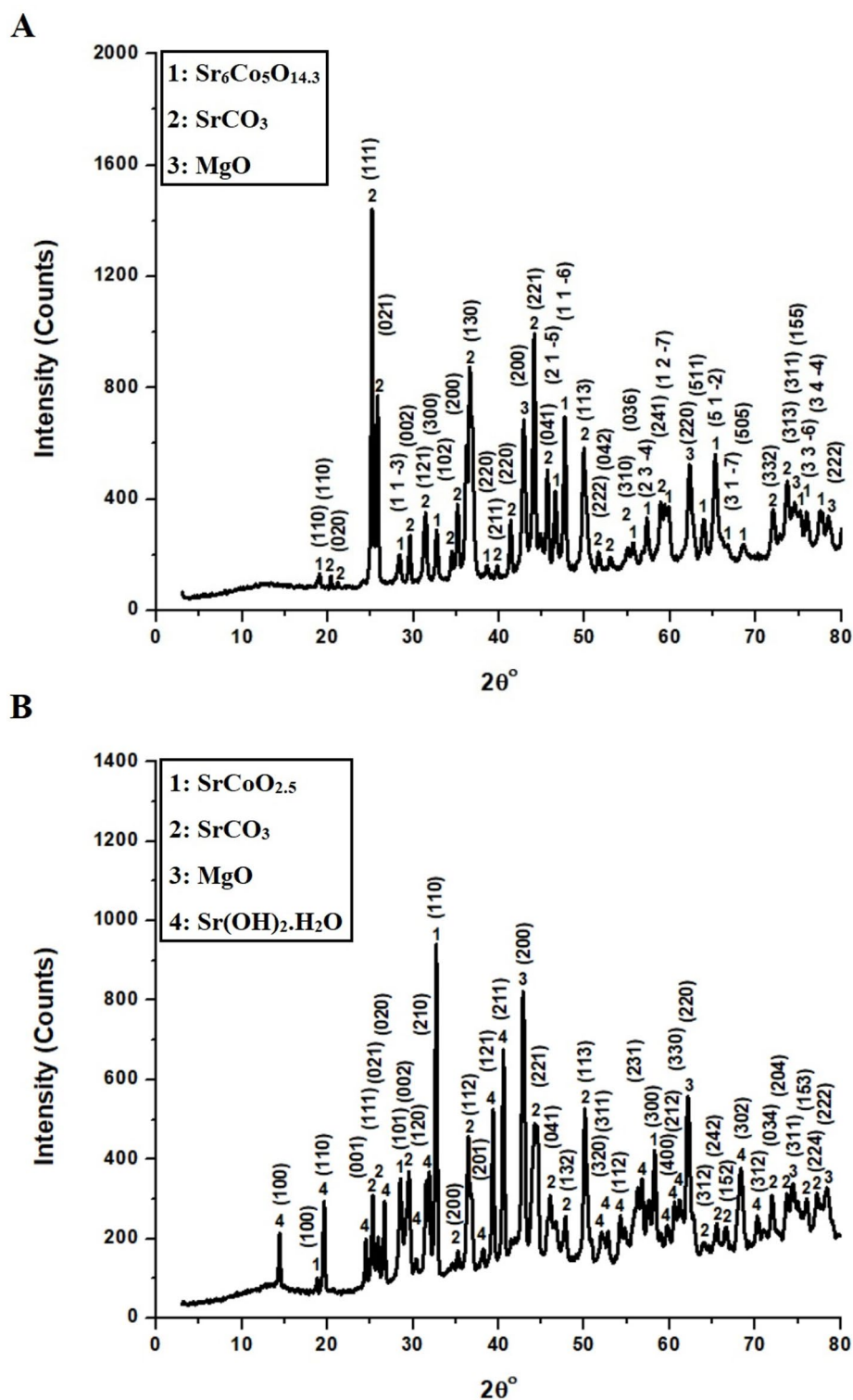


Fig. 2. XRD diffractograms of (A) MSC600 and (B) MSC800 nanohybrids.

(310), (241), (332), and (313) planes, respectively. The cubic MgO in MSC600 exhibits diffraction maxima at 2θ values of 42.91, 62.23, 74.51, and 78.51 assigned to the (200), (220), (311), and (222) planes, respectively. For the MSC800 nanocomposite, Fig. 2B confirms the formation of hexagonal $\text{SrCoO}_{2.5}$ identified by card JCPDS 00 048 0875, orthorhombic SrCO_3 identified by card JCPDS 01 071 2393, cubic MgO identified by card JCPDS 01 087 0653, and orthorhombic $\text{Sr}(\text{OH})_2 \cdot \text{H}_2\text{O}$ identified by card JCPDS 00 028 1222. The hexagonal $\text{SrCoO}_{2.5}$ phase displays reflections at 2θ values of 18.75, 28.56, 32.69, and 58.23, which can be attributed to the (100), (101), (110), and (300) planes, respectively. The orthorhombic SrCO_3 in MSC800 yields peaks at 2θ values of

25.24, 25.93, 29.52, 35.17, 36.42, 44.29, 46.09, 47.88, 50.09, 64.02, 65.53, 66.51, 71.89, 73.81, 76.04, and 77.26 that match the (111), (021), (002), (200), (112), (221), (041), (132), (113), (312), (242), (152), (034), (204), (153), and (224) planes, respectively. The cubic MgO phase in MSC800 produces diffraction peaks at 2θ values of 42.91, 62.23, 74.37, and 78.38, which correspond to the (200), (220), (311), and (222) planes, respectively. The $\text{Sr}(\text{OH})_2 \cdot \text{H}_2\text{O}$ is characterized by reflections at 2θ values of 14.34, 19.59, 24.42, 26.63, 30.34, 31.87, 38.21, 39.32, 40.56, 52.02, 52.69, 54.23, 56.72, 59.61, 60.57, 61.12, 68.30, and 70.22 indexed to the (100), (110), (001), (020), (120), (210), (201), (121), (211), (320), (311), (112), (231), (400), (212), (330), (302), and (312) planes, respectively. The average crystallite size is 58.12 nm for MSC600 and 68.62 nm for MSC800, and the larger crystallites in MSC800 are ascribed to the elevated calcination temperature, which enhances crystallinity, promotes grain growth, and leads to coarsening of the crystalline domains.

A clearer comparison between MSC600 and MSC800 reveals that MgO and SrCO_3 remain present in both nanohybrids, whereas the Sr–Co oxide phase changes from rhombohedral $\text{Sr}_6\text{Co}_5\text{O}_{14.3}$ in MSC600 to hexagonal $\text{SrCoO}_{2.5}$ in MSC800, indicating that increasing the calcination temperature promotes a clear phase rearrangement within the strontium–cobalt oxide framework. In addition, the increase in average crystallite size from 58.12 nm for MSC600 to 68.62 nm for MSC800 confirms improved crystal growth at the higher calcination temperature. The appearance of $\text{Sr}(\text{OH})_2 \cdot \text{H}_2\text{O}$ in MSC800 may be related to the distinct phase evolution pathway promoted at 800 °C in the Pechini-derived precursor system. In the present synthesis route, tartaric acid and polyethylene glycol 400-assisted polymeric complexation likely ensured intimate cation distribution at the molecular level; therefore, increasing the calcination temperature to 800 °C induced a deeper rearrangement of the Sr-containing species and led to the formation of an additional strontium-based crystalline phase not detected in MSC600. Thus, the emergence of $\text{Sr}(\text{OH})_2 \cdot \text{H}_2\text{O}$ is more reasonably associated with the temperature-dependent phase evolution of Sr-rich domains in this multicomponent Pechini system than with a simple direct thermal formation of a hydroxide phase. Therefore, the XRD results verify not only the phase content of the prepared products, but also the temperature-driven alteration in their crystalline characteristics.

Semiquantitative XRD analysis further clarified the phase ratios in the synthesized nanohybrids. MSC600 was found to consist of approximately 5% $\text{Sr}_6\text{Co}_5\text{O}_{14.3}$, 81% SrCO_3 , and 14% MgO, whereas MSC800 consisted of about 53% $\text{SrCoO}_{2.5}$, 7% SrCO_3 , 14% MgO, and 26% $\text{Sr}(\text{OH})_2 \cdot \text{H}_2\text{O}$. These results confirm that the two nanohybrids are not only different in phase identity, but also markedly different in phase proportion, which further supports the strong influence of calcination temperature on phase evolution in the present Pechini-derived system.

EDX

Figure 3 together with Table 2, shows that both MSC600 (Fig. 3A) and MSC800 (Fig. 3B) exhibit characteristic EDS peaks of C, Mg, O, Co, and Sr, which confirms the successful formation of multicomponent. The carbon signal in both spectra originates mainly from incomplete decomposition of the organic precursors used in the Pechini sol-gel process, where tartaric acid acts as a chelating agent and polyethylene glycol 400 forms a polymeric network that can leave residual carbonaceous species and surface carbonate groups. The more intense carbon contribution in MSC800 compared with MSC600 reflects the accumulation of carbon-containing species at the surface of the strontium-rich phases and the surface sensitivity of EDS, which preferentially detects these species even when the overall bulk composition is largely inorganic oxide. The difference in atomic percentages between MSC600 and MSC800 arises from thermally driven phase transformations, cation diffusion, and grain growth at the higher calcination temperature, which promote segregation of strontium-rich phases toward the particle surface while magnesium and cobalt become more homogeneously distributed within the bulk so that the surface sampled by EDS appears enriched in strontium and relatively depleted in magnesium and cobalt. Overall, Fig. 3; Table 2 demonstrate that the Pechini sol-gel route with polyethylene glycol 400 and tartaric acid produces chemically integrated oxide nanocomposites whose apparent elemental composition is strongly influenced by the calcination temperature and the associated changes in surface phases and microstructure.

FE-SEM

Figure 4A shows the FE-SEM image of the MSC600 sample and reveals that the surface is built from numerous rod-like and needle-like crystallites, which intersect and interlock to form an open porous network. These elongated particles can be described as rods and short nanorods and some irregular plate-like grains that grow preferentially along specific crystallographic directions during the Pechini sol-gel synthesis at the lower calcination temperature. In contrast, Fig. 4B presents the FE-SEM image of the MSC800 sample and displays a compact layer of closely packed, nearly spherical and irregular polyhedral nanoparticles that are strongly agglomerated and fill most of the available voids. This granular morphology in MSC800 arises from enhanced atomic diffusion and sintering at the higher calcination temperature, which promote coalescence of the initial rods into larger aggregates and drive recrystallization toward more isotropic particle shapes. Thus, Fig. 4A and B together demonstrate that increasing the calcination temperature in the Pechini sol-gel route transforms the nanocomposite morphology from rod-like and needle-like structures to dense clusters of spherical and polyhedral nanoparticles as grain growth and phase evolution progressively erase the original anisotropic features.

HR-TEM

Figure 5 presents HR-TEM images of the MSC600 (Fig. 5A) and MSC800 (Fig. 5B) products and reveals clear differences in their morphology. In Fig. 5A, the MSC600 sample appears as a rod-like or wire-like aggregate that is densely built from tightly packed, nearly spherical and short polyhedral nanocrystals, which form a continuous chain of fine grains along the longitudinal direction of the rod. In Fig. 5B, the MSC800 product is composed of larger, nearly spherical, and well-faceted polyhedral particles together with a few onion-like or

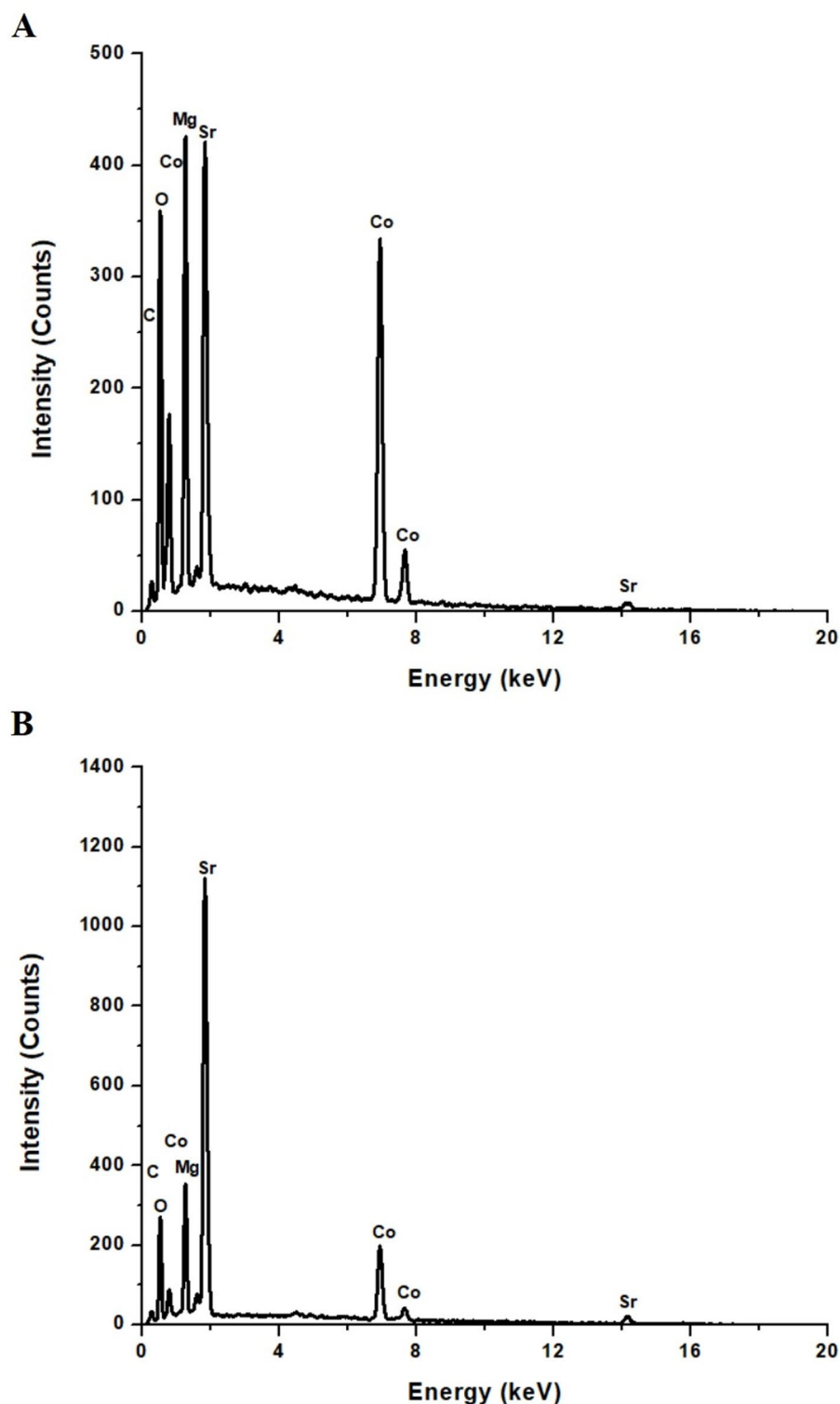


Fig. 3. EDS patterns of (A) MSC600 and (B) MSC800 nano-hybrids.

core-shell particles that exhibit concentric contrast, and these particles are more discrete and less densely packed than those observed for MSC600. The evolution from a rod-like assembly of small nanocrystals in MSC600 to larger isolated spherical and polyhedral grains in MSC800 is attributed to the higher calcination temperature that enhances atomic diffusion, promotes coalescence and recrystallization of the primary nuclei, and allows thermodynamically favored low-energy facets to develop, which results in grain growth and partial loss of the original anisotropic framework produced by the Pechini sol-gel synthesis.

Nanohybrid	Atomic percentages				
	% C	% O	% Mg	% Co	% Sr
MSC600	6.1	48.1	18.0	19.9	7.9
MSC800	9.8	50.0	11.3	10.5	18.4

Table 2. Elemental composition of MSC600 and MSC800 nanohybrids.

Beyond the morphological differences, the HR-TEM images also suggest the multiphase character of both nanohybrids. The presence of nanodomains with different contrast levels and distinct local particle geometries, together with the visible junctions between adjacent crystalline regions, indicates that the products are not composed of a single uniform phase. Instead, these features are consistent with the coexistence of multiple phases and the formation of interfacial boundaries between neighboring domains within the nanohybrid structure. Such interphase contact regions are expected in the present materials because the XRD analysis confirmed the presence of several crystalline components in each sample.

Optimization

Impact of pH variation on removal performance

Figure 6 shows that basic red 9 removal is very low under strongly acidic conditions since at pH 2 the MSC600 nanohybrid eliminates only 2.41% of the basic red 9 dye while MSC800 eliminates 1.68%, and this indicates that both surfaces are unfavorable for uptake at low pH. When the pH is raised to 10, Fig. 6 records a marked increase in dye removal since MSC600 reaches 94.53% and MSC800 reaches 67.23%, which means that both nanocomposites become highly effective adsorbents in alkaline media, with MSC600 clearly outperforming MSC800.

Mechanism of adsorption Figure 7 reveals that the pH_{PZC} of MSC600 is 7.32 and that of MSC800 is 8.52, so at pH equals 2, the dye solution pH is well below pH_{PZC} for each material, and the surfaces carry a net positive charge, which corresponds to the situation illustrated in Fig. 8 under conditions where $pH < pH_{PZC}$, where protonated surface sites experience electrostatic repulsion toward the cationic basic red 9 species, and adsorption is therefore strongly hindered. At pH 10, the dye solution pH is higher than the pH_{PZC} of both nanohybrids, and Fig. 8 represents this case of $pH > pH_{PZC}$, where deprotonation of surface hydroxyl groups generates negatively charged sites that attract the positively charged basic red 9 ions through strong electrostatic forces, and this attraction explains the high removal efficiencies observed. The difference between the two samples can be interpreted by noting that pH 10 lies further above the pH_{PZC} of MSC600 than above that of MSC800, so the surface of MSC600 becomes more negatively charged, which enhances electrostatic attraction toward the dye and yields a higher removal percentage compared with MSC800 under the same conditions.

To clarify the adsorption mechanism, FT-IR analysis was performed on the MSC600 sample before (Fig. 9A) and after the adsorption of basic red 9 dye (Fig. 9B) as an illustrative example. The results shown in Fig. 9 clearly confirm the involvement of several functional groups and active sites in the removal process. Before adsorption, the bands at 399, 557, and 661 cm^{-1} are assigned to metal–oxygen vibrations (Sr–O, Co–O, and Mg–O), confirming the presence of metal-based active centers that can participate in surface complexation, while the band at 861 cm^{-1} is attributed to carbonate species and the bands at 1075 and 1447 cm^{-1} are related to C–O and carbonate-associated vibrations, indicating the presence of oxygen-containing groups that can act as negatively charged or polar adsorption sites. The band at 1772 cm^{-1} is assigned to C=O stretching of carbonyl groups, which can serve as hydrogen-bonding sites. After adsorption, the retention of the main structural bands indicates that the framework of MSC600 remained stable, whereas the shift of the band from 1075 to 1068 cm^{-1} and the appearance of new bands at 943, 1040, 1143, 1253, 1357, and 1592 cm^{-1} confirm the successful attachment of basic red 9 molecules onto the adsorbent surface. These newly appeared bands are associated with the organic structure of the dye, particularly C–N, C–C, and aromatic C=C/N–H vibrations, verifying that the dye molecules were immobilized on MSC600. The appearance of the band at 1592 cm^{-1} particularly supports the occurrence of π - π interaction between the aromatic rings of the dye and the carbonaceous domains of the adsorbent, while the shift in the oxygen-containing band demonstrates the involvement of C–O/carbonate groups in the adsorption process^{73,74,77}. Therefore, the FT-IR results in Fig. 9 demonstrate that the adsorption of basic red 9 onto MSC600 proceeded through a synergistic mechanism involving electrostatic interactions between the cationic dye and negatively charged oxygenated sites, hydrogen bonding through carbonyl and other oxygen-containing groups, π - π interaction with the carbon phase, and surface complexation through the metal–oxygen active centers as shown in Fig. 8.

The N_2 adsorption-desorption isotherms presented in Fig. 10A confirm that both MSC600 and MSC800 possess accessible porous structures, while the pore size distribution curves in Fig. 10B demonstrate that the porosity is mainly associated with wide textural pores and interparticle voids. As listed in Table 3, MSC600 exhibits a higher BET surface area (1.78 m^2/g), larger total pore volume ($4.65 \times 10^{-2} cm^3/g$), and greater mean pore diameter (105.34 nm) than MSC800, which shows corresponding values of 1.46 m^2/g , $3.57 \times 10^{-2} cm^3/g$, and 96.83 nm. These findings indicate that calcination at 600 °C preserves a more open and less compact texture, whereas calcination at 800 °C promotes particle growth, aggregation, and partial densification, leading to a reduction in the accessible surface area and pore volume. The relatively large pore diameters of both nanohybrids suggest that the porous system is dominated by intergranular/macroporous channels rather than fine micropores, which is beneficial for facilitating the diffusion of bulky basic red 9 molecules toward the active adsorption sites.

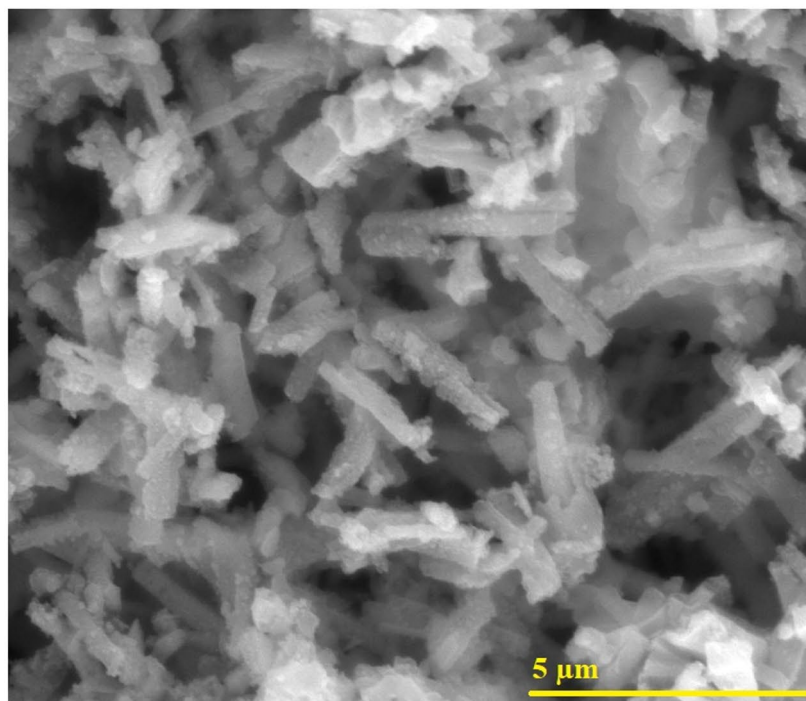
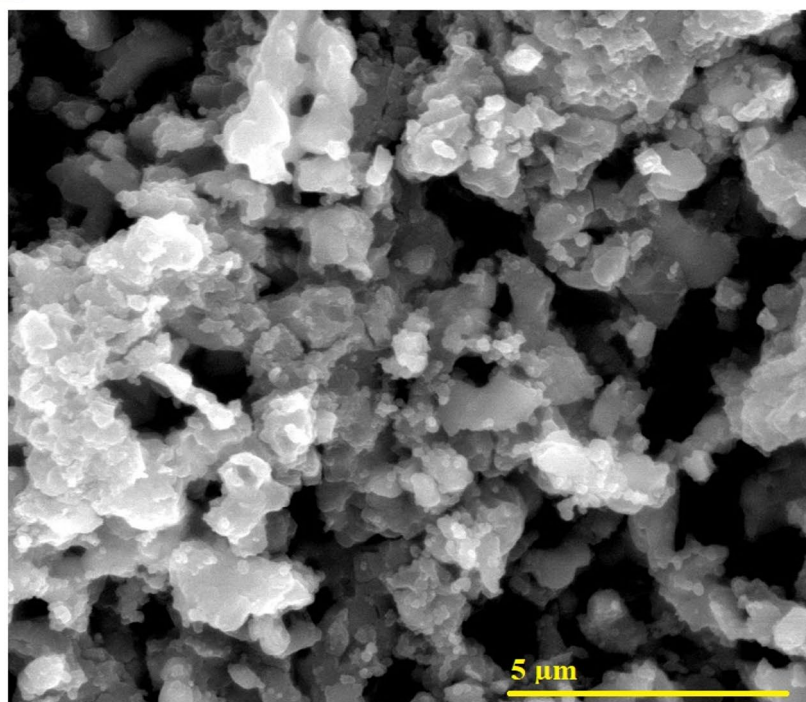
A**B**

Fig. 4. FE-SEM images of (A) MSC600 and (B) MSC800 nanohybrids.

Therefore, the better textural properties of MSC600 provide a more favorable pathway for mass transfer and greater exposure of adsorption centers, which contributes to its superior adsorption performance compared with MSC800.

Impact of contact time on adsorption efficiency

Figure 11 illustrates that the uptake of basic red 9 dye utilizing MSC600 and MSC800 rises speedily at the beginning of contact, then slowly levels off as the systems approach equilibrium. For MSC600, the removal

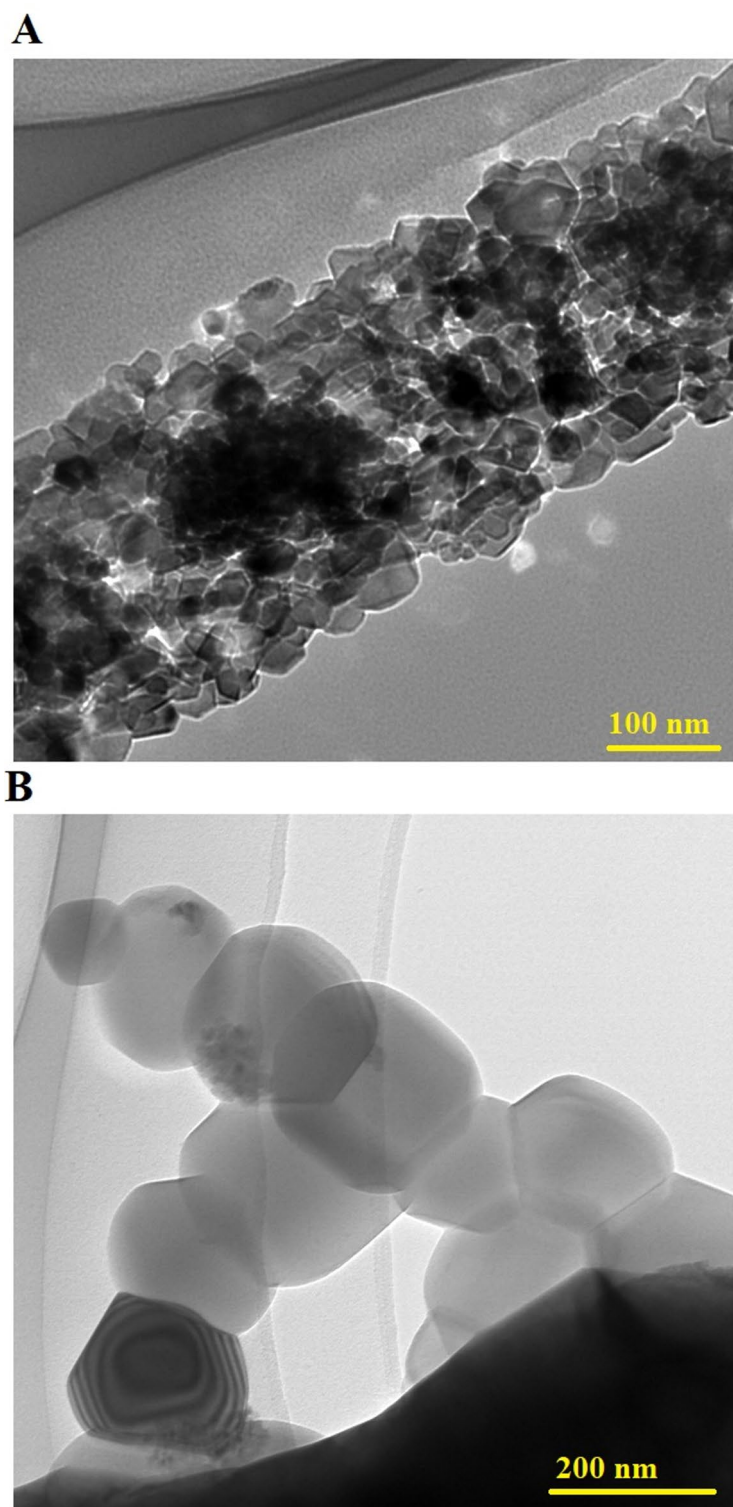


Fig. 5. HR-TEM images of (A) MSC600 and (B) MSC800 nano hybrids.

efficacy is 45.49% after 10 min and reaches 94.41% at 60 min, which is the equilibrium time, showing that most adsorption sites are already occupied and that extending the contact time beyond this point does not yield additional removal because the surface is essentially saturated. For MSC800, the removal is 27.96% at 10 min and rises to 67.06% at 80 min, which represents its equilibrium time, indicating a slower approach to saturation and a lower ultimate uptake for this nanocomposite relative to MSC600. Overall, Fig. 10 demonstrates that both materials display rapid initial adsorption followed by a plateau associated with saturation of active sites, while

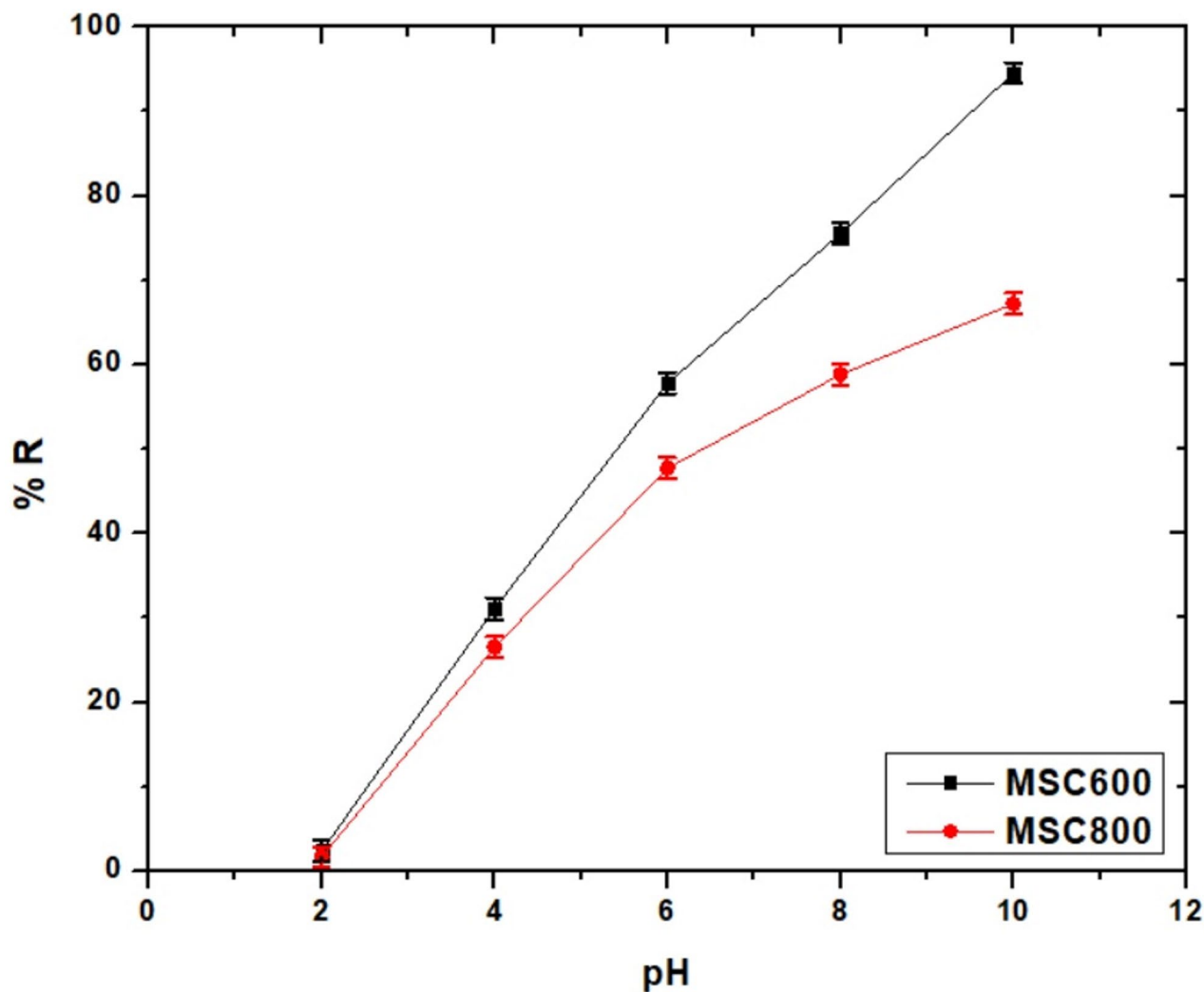


Fig. 6. Impact of pH on the removal efficiency of basic red 9 using MSC600 and MSC800 nano hybrids.

MSC600 attains higher dye removal within a shorter contact time than MSC800, confirming its stronger affinity toward basic red 9 under the investigated conditions.

Figure 12A–B presents kinetic plots for basic red 9 elimination on MSC600 and MSC800 that were examined employing the pseudo-first-order kinetic model described by Eq. (5) and the pseudo-second-order kinetic model described by Eq. (6)^{78–80}, and the corresponding kinetic parameters are reported in Table 4.

$$\log(Q_e - Q_t) = \log Q_e - \frac{K_1}{2.303}t \quad (5)$$

$$\frac{t}{Q_t} = \frac{1}{K_2 Q_e^2} + \frac{1}{Q_e}t \quad (6)$$

In these equations, Q_e denotes the adsorption capacity at equilibrium, Q_t denotes the adsorption capacity at time t , K_1 represents the pseudo first-order rate constant, and K_2 represents the pseudo second-order rate constant.

Analysis of Fig. 12 in conjunction with the kinetic parameters in Table 4 shows that the adsorption of basic red 9 on MSC600 and MSC800 follows the pseudo-first-order model because the Q_e values obtained from this model agree closely with the experimental capacity Q_{Exp} , and the corresponding R^2 values reach 0.9999, which is higher than those ascribed to the pseudo-second-order model.

Impact of temperature on adsorption efficiency

Figure 13 indicates that basic red 9 removal decreases as the temperature increases from 298 K to 328 K for both MSC600 and MSC800, which means that adsorption becomes less favorable at higher temperatures. At 298 K, MSC600 exhibits a removal efficiency of 94.41%, whereas MSC800 exhibits 67.06%, showing that MSC600 has a higher adsorption efficiency at room temperature. Increasing the temperature to 328 K reduced the removal to 88.42% for MSC600 and 59.50% for MSC800, so both materials lose part of their uptake capacity, although

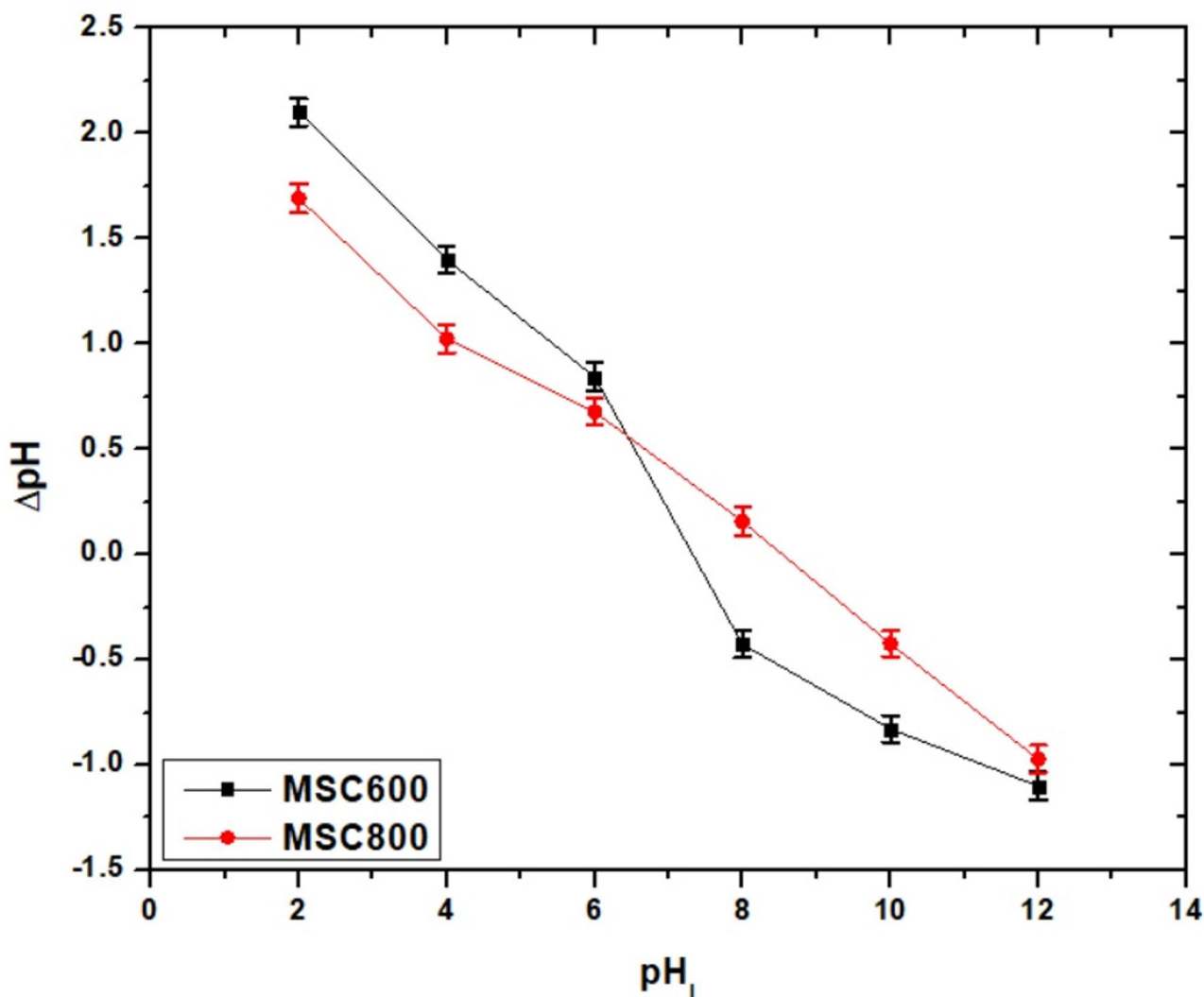


Fig. 7. pH_{PZC} of MSC600 and MSC800 nano hybrids.

MSC600 still outperforms MSC800 at the higher temperature. Overall, Fig. 13 demonstrates that the two nanocomposites follow the same trend of reduced dye removal with increasing temperature, while MSC600 consistently exhibits superior performance compared with MSC800 at both 298 K and 328 K.

Figure 14, together with the thermodynamic parameters in Table 5, shows that basic red 9 adsorption on MSC600 and MSC800 was evaluated using the Van't Hoff relationship and related thermodynamic expressions. The calculations were carried out using Eqs. (7), (8), and (9)^{81,82}.

$$\ln K_d = \frac{\Delta S^{\circ}}{R} - \frac{\Delta H^{\circ}}{RT} \quad (7)$$

$$K_d = \frac{Q_e}{C_e} \quad (8)$$

$$\Delta G^{\circ} = \Delta H^{\circ} - T\Delta S^{\circ} \quad (9)$$

In these equations, ΔH° is the standard enthalpy change, ΔS° is the standard entropy change, ΔG° is the standard Gibbs free energy change, R is the universal gas constant, T is the absolute temperature in kelvin, and K_d is the distribution coefficient.

Table 5 indicates that ΔH° values are lower than 40 kJ/mol and negative, and ΔG° values are also negative, while ΔS° values are positive, so elimination of basic red 9 utilizing both MSC600 and MSC800 nano hybrids is physical, exothermic, spontaneous, and thermodynamically feasible.

Influence of concentration variation on adsorption performance

Figure 15 reveals that increasing the initial basic red 9 concentration progressively lowers the removal efficiency for both MSC600 and MSC800 nanocomposites. At 100 mg/L, MSC600 removes 98.44% of the basic red 9 dye,

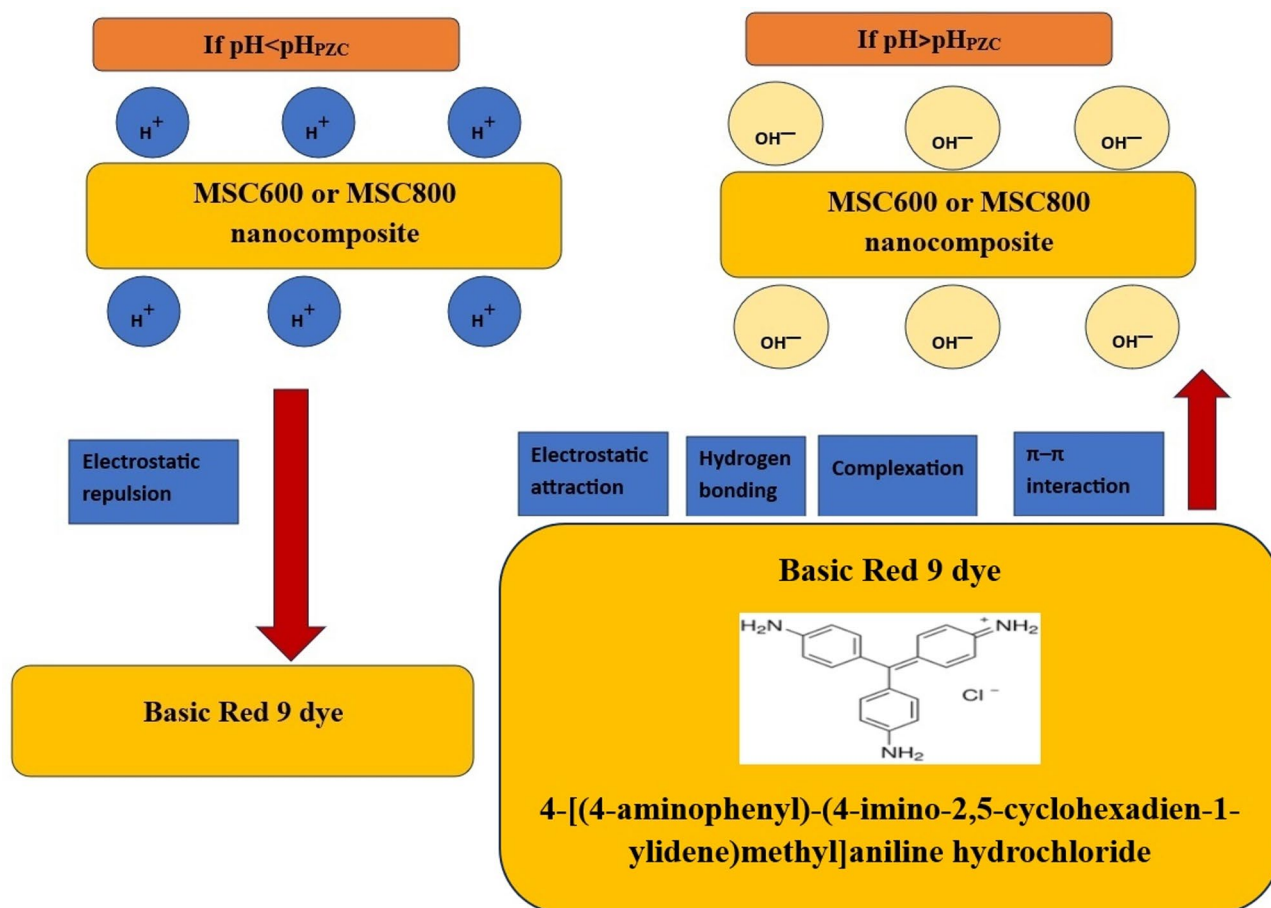


Fig. 8. Removal mechanism of basic red 9 using MSC600 and MSC800 nano hybrids.

whereas MSC800 exhibits 94.52%, which reveals almost complete decolorization at low concentration. When the initial concentration rises to 400 mg/L, the removal decreases to 71.12% for MSC600 and 50.73% for MSC800, showing that many active sites become saturated, and a larger fraction of dye remains in solution. Comparison of these two concentrations therefore demonstrates that MSC600 consistently exhibits higher removal than MSC800 and that the adsorption efficiency of both materials is more effectively exploited at lower basic red 9 loadings.

Equilibrium adsorption results for basic red 9 on MSC600 and MSC800 were fitted to the equilibrium Langmuir isotherm described via Eq. (10)^{83,84}. The same data were also analyzed with the Freundlich model using Eqs. (11) and (12)^{85–87}.

$$\frac{C_e}{Q_e} = \frac{1}{K_3 Q_{\max}} + \frac{C_e}{Q_{\max}} \quad (10)$$

$$\ln Q_e = \ln K_4 + \frac{1}{n} \ln C_e \quad (11)$$

$$Q_{\max} = K_4 (C_o^{1/n}) \quad (12)$$

In these equations, Q_{\max} refers to the maximum monolayer capacity, Q_e refers to the equilibrium adsorption capacity, K_3 denotes the Langmuir affinity constant, K_4 refers to the Freundlich constant, and n is the Freundlich heterogeneity factor.

The linear plots in Fig. 16A,B, together with the isotherm constants in Table 6, show that the Langmuir representation gives higher R^2 values, so adsorption of basic red 9 follows the Langmuir isotherm for both nanocomposites.

Table 7 summarizes the maximum adsorption capacities (Q_{\max}) for basic red 9 obtained with several reference adsorbents and with the MSC600 and MSC800 nanocomposites. Literature materials such as activated carbon, lignocellulose, biochar, and rice husk show relatively low Q_{\max} values in the range of 7.20 to 69.82 mg/g. In contrast, MSC600 and MSC800 reach Q_{\max} values of 436.68 and 313.48 mg/g, which clearly demonstrates their much higher affinity toward basic red 9 dye. This superior performance arises from a synergistic effect generated

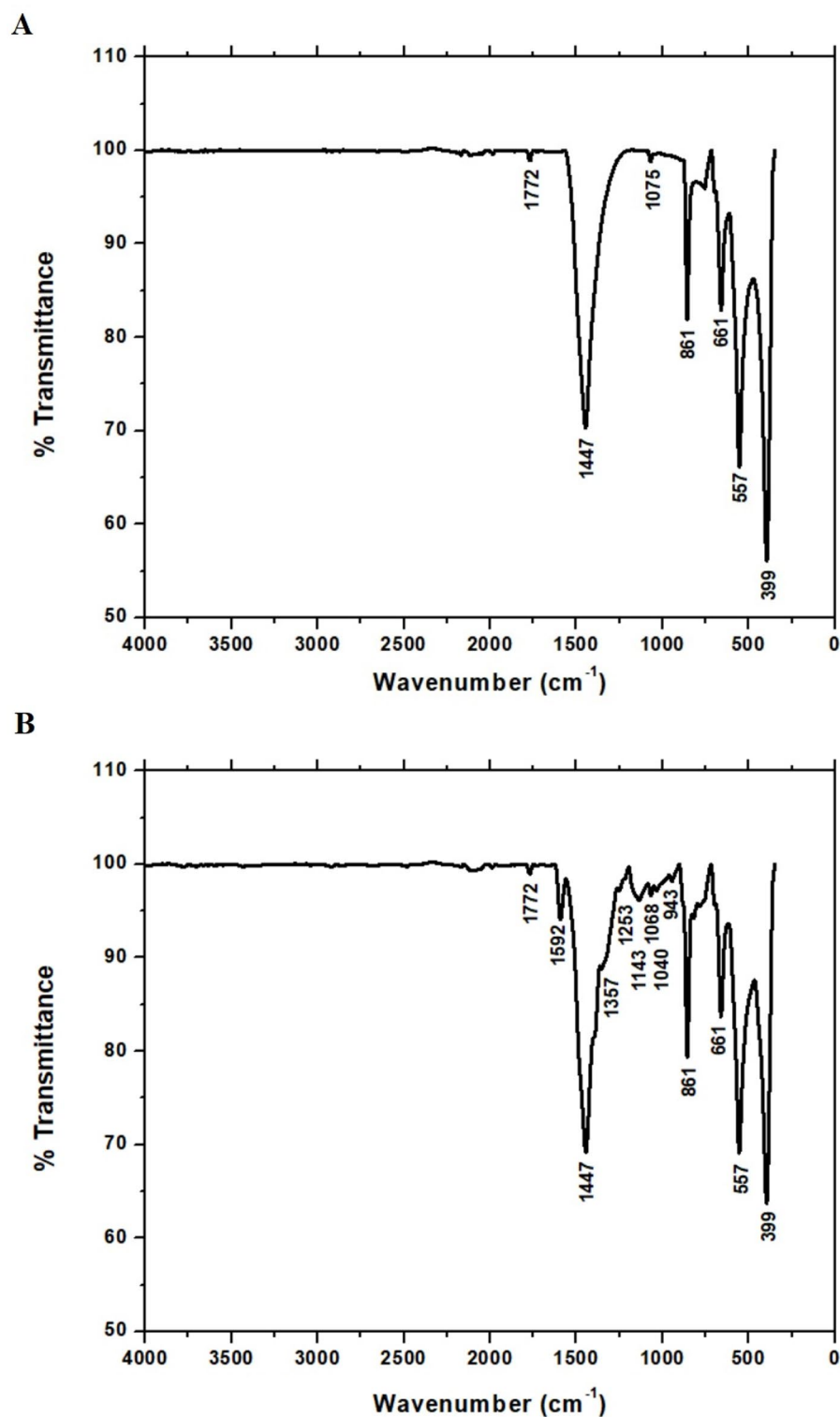


Fig. 9. FT-IR spectra of MSC600 (A) before and (B) after adsorption of basic red 9 dye.

by the presence of multiple crystalline phases within each nanocomposite that creates more heterogeneous active sites and promotes stronger interactions between the adsorbent surface and dye molecules.

Regeneration/reuse studies

Figure 17 shows that the percentage desorption of basic red 9 increases steadily with increasing hydrochloric acid concentration for both MSC600 and MSC800 nanocomposites. At 1 M HCl, the desorption of basic red 9 reaches 86.79% for MSC600 and 82.63% for MSC800, indicating efficient dye release under moderately acidic

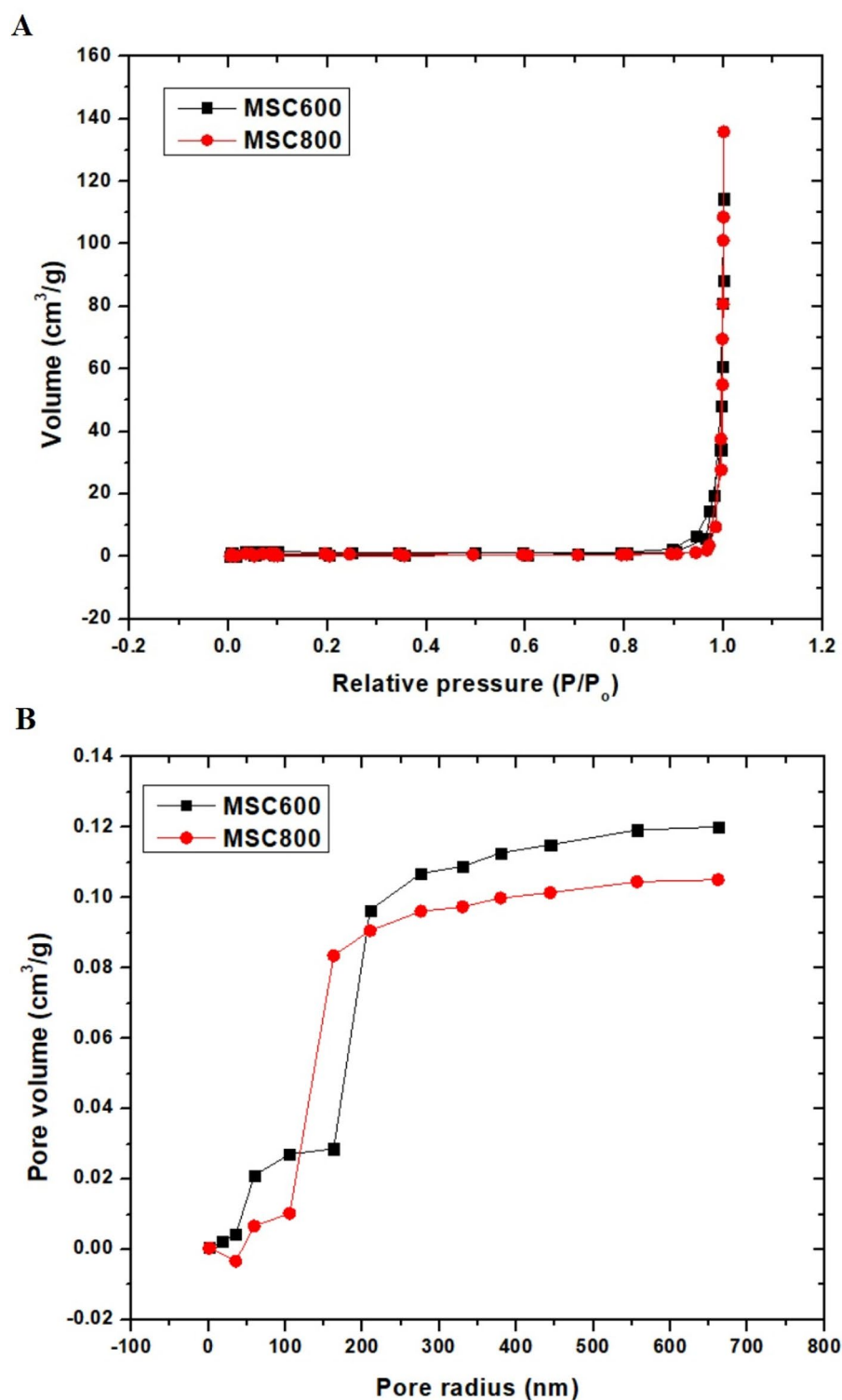


Fig. 10. (A) N₂ adsorption/desorption isotherms and (B) Pore size distribution curves of MSC600 and MSC800 nano hybrids.

conditions. When the HCl concentration is raised to 1.5 M and 2 M, the desorption efficiencies increase to 94.47% and 99.79% for MSC600 and to 92.05% and 99.41% for MSC800, which means that almost complete dye removal from the surface is achieved at the highest acid concentration. Hydrochloric acid provides excellent desorption because abundant H⁺ ions protonate the surface sites and weaken the electrostatic attraction between the positively charged basic red 9 molecules and the nanocomposite surface, while competitive binding of

Sample	MSC600	MSC800
BET surface area (m ² /g)	1.78	1.46
Total pore volume (cm ³ /g)	4.65 × 10 ⁻²	3.57 × 10 ⁻²
Mean pore diameter (nm)	105.34	96.83

Table 3. Surface textures of MSC600 and MSC800 nano hybrids.

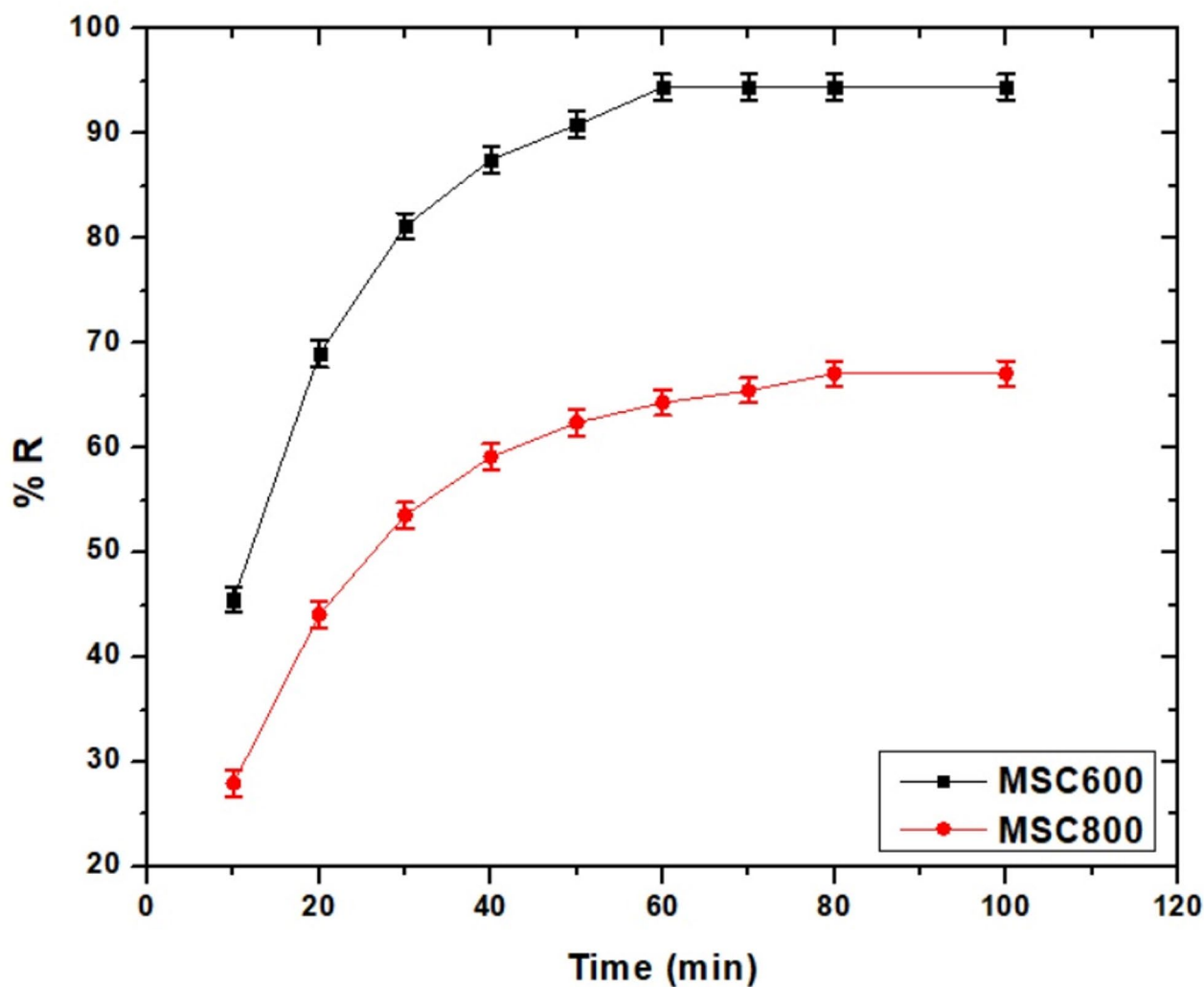


Fig. 11. Time-dependent elimination of basic red 9 by MSC600 and MSC800 nano hybrids.

protons to these sites displaces the dye back into solution and restores the adsorption capacity of the regenerated materials.

Figure 18 shows that repeated adsorption-desorption cycles lead to a gradual decrease in the removal efficiency of basic red 9 dye for both MSC600 and MSC800 nanocomposites. For MSC600, the removal efficiency is 94.41% in cycle 0 and decreases only slightly with each regeneration step until it reaches 89.39% in cycle 5, which indicates good retention of adsorption performance. For MSC800, the basic red 9 removal starts at 67.06% in cycle 0 and then progressively declines to 58.76% in cycle 5, showing a greater loss in performance than that observed for MSC600. Overall, Fig. 18 demonstrates that both nanocomposites remain reusable over several cycles, although MSC600 maintains a higher and more stable removal efficiency than MSC800 throughout the regeneration sequence.

To further confirm the structural stability of the synthesized nano hybrid after repeated use, the filtrate obtained after the adsorption/desorption experiments was analyzed by inductively coupled plasma, and the results revealed that no Sr, Co, or Mg ions were detected, confirming the absence of measurable metal leaching from the adsorbent. In addition, to provide direct evidence for the preservation of the crystal structure, XRD analysis was performed on the regenerated MSC600 sample as an illustrative example after the fifth regeneration

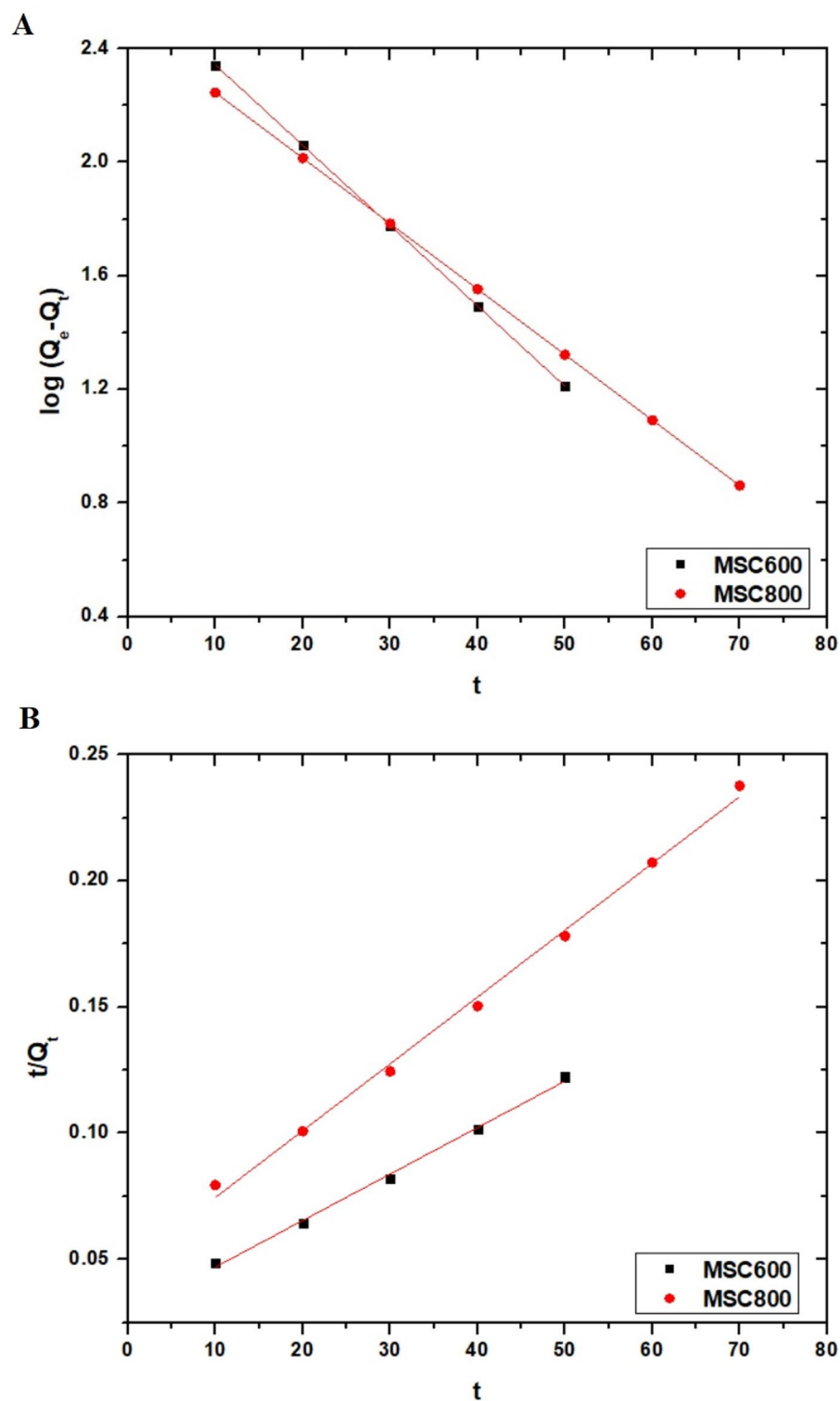


Fig. 12. (A) Pseudo-first-order and (B) pseudo-second-order models.

cycle. As shown in Fig. 19, the diffraction pattern of the regenerated MSC600 remains highly consistent with that of the fresh MSC600 presented in Fig. 2A, with the characteristic diffraction peaks of the main phases still clearly retained and without the appearance of obvious new peaks related to structural decomposition or undesirable phase transformation. This strong similarity between Figs. 2A and 19 demonstrates that the crystalline framework of MSC600 was well preserved during the repeated adsorption–desorption cycles, thereby confirming the excellent structural stability and reusability of the prepared nanohybrid.

Nanohybrid	Q_{Exp} (mg/g)	Pseudo-1st -order		Pseudo-2nd -order			
		K_1 (1/min)	R^2	Q_c (mg/g)	K_2 (g/mg.min)	R^2	Q_c (mg/g)
MSC600	424.86	0.06527	0.9999	422.73	0.000118	0.9959	543.48
MSC800	301.77	0.05318	0.9999	299.45	0.000576	0.9957	377.36

Table 4. Kinetic constants for basic red 9 elimination using MSC600 and MSC800 nanohybrids.

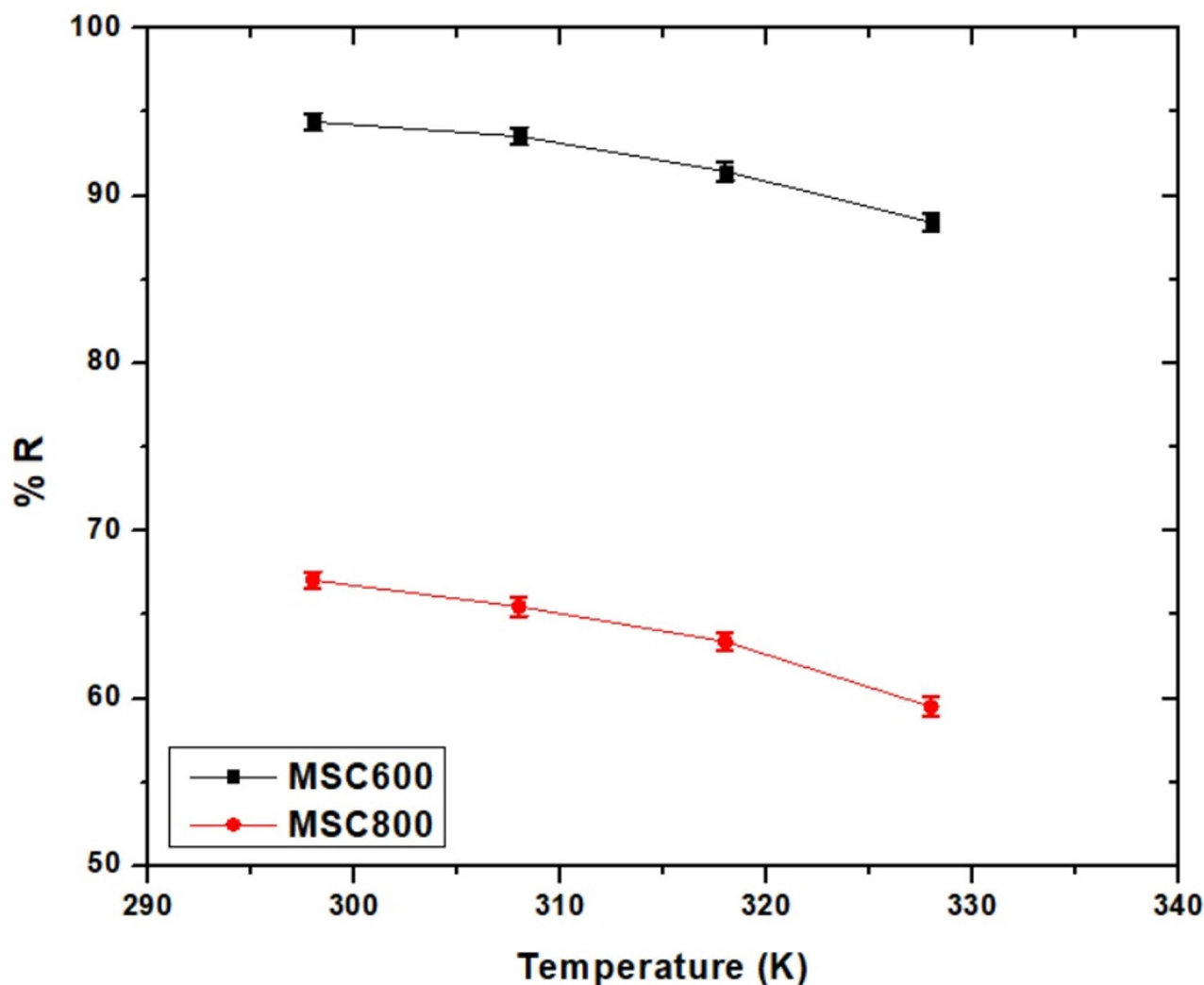


Fig. 13. Impact of solution temperature on the elimination percentage of basic red 9 by MSC600 and MSC800 nanohybrids.

Effect of interference

The impact of coexisting ions and competing dyes on basic red 9 uptake by MSC600 and MSC800 was assessed under identical conditions, and the results are presented in Table 8. Monovalent cations and anions such as Na^+ , K^+ , Cl^- , and NO_3^- cause only slight decreases in adsorption capacity, which indicates that both nanocomposites tolerate the presence of simple electrolytes. Divalent cations, Mg^{2+} and Ca^{2+} , produce a clearly stronger reduction in uptake because their higher charge density allows them to occupy and shield negatively charged surface sites that would otherwise bind basic red 9. The largest losses in capacity occur in the presence of methylene blue and crystal violet, which strongly compete for the same adsorption sites, yet MSC600 still maintains higher adsorption capacities than MSC800 and therefore shows better performance in complex solutions.

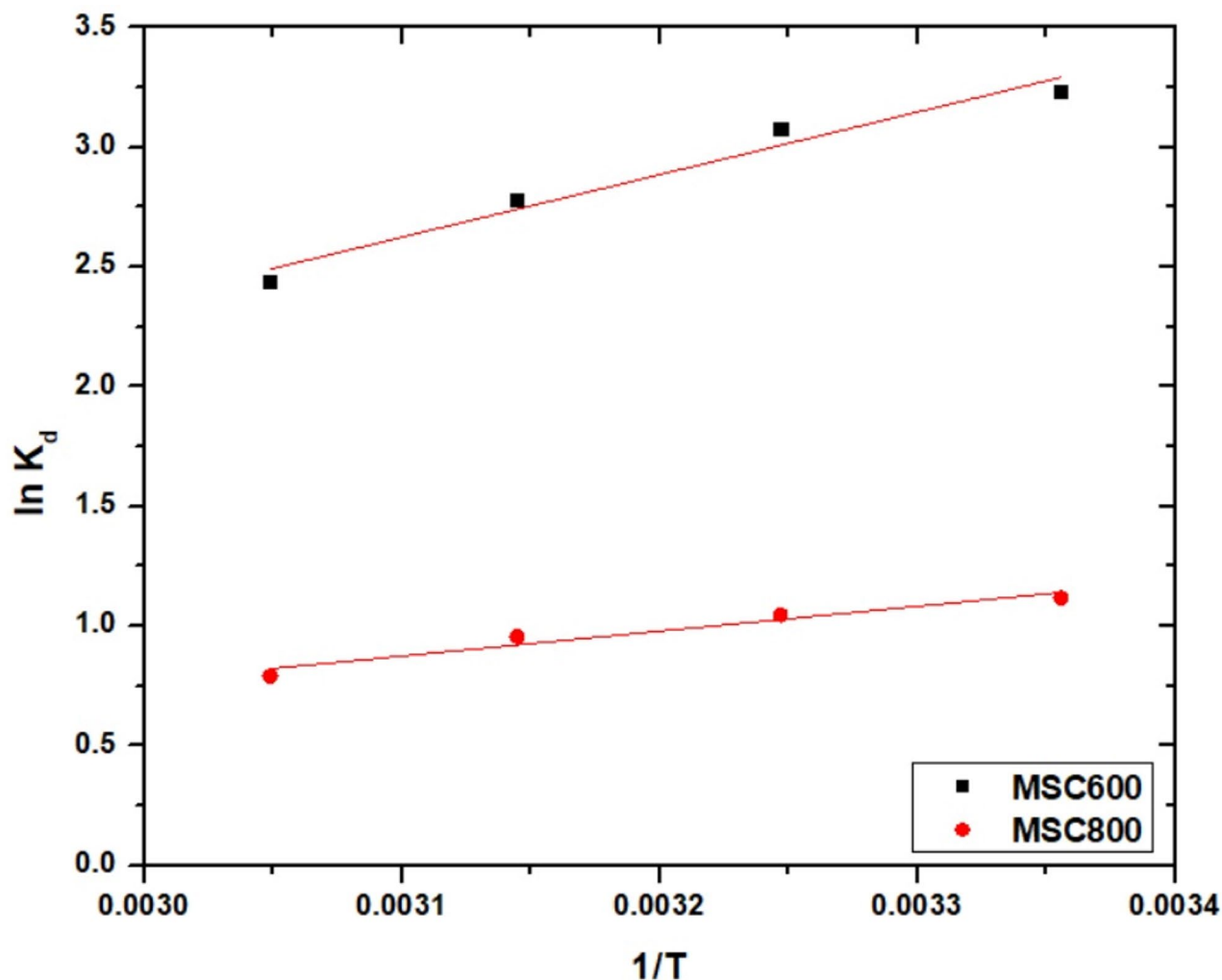


Fig. 14. Van't Hoff plots of $\ln K_d$ against $1/T$ for basic red 9 elimination utilizing MSC600 and MSC800 nano hybrids.

Nano hybrid	ΔS° (kJ/mol.K)	ΔH° (kJ/mol)	ΔG° (kJ/mol)			
			298 K	308 K	318 K	328 K
MSC600	0.04576	-21.84	-35.47	-35.93	-36.39	-36.84
MSC800	0.01961	-8.68	-14.53	-14.73	-14.92	-15.12

Table 5. Thermodynamic constants for basic red 9 elimination utilizing MSC600 and MSC800 nano hybrids.

Assessment of basic red 9 removal from wastewater

To better examine the real-world applicability of the prepared nano hybrids, separation tests were performed using an actual wastewater effluent collected from the undergraduate chemistry teaching laboratories at the College of Science, Imam Mohammad Ibn Saud Islamic University (Riyadh, Saudi Arabia). Prior to the adsorption runs, the sample was fortified with basic red 9 to set the initial dye level at 300 mg/L, thereby aligning it with the concentration applied in the single-component synthetic trials while maintaining the native ionic background of the real matrix. Analysis of the spiked effluent confirmed the presence of typical inorganic constituents arising from routine student laboratory activities, including K^+ (12.7 mg/L), Na^+ (58.4 mg/L), Ca^{2+} (24.3 mg/L), Mg^{2+} (7.9 mg/L), NO_3^- (21.6 mg/L), Cl^- (71.5 mg/L), SO_4^{2-} (46.2 mg/L), HCO_3^- (118.0 mg/L), and PO_4^{3-} (4.6 mg/L). In addition, only trace concentrations of metals were detected, namely Cu (0.06 mg/L), Fe (0.23 mg/L), and Zn (0.11 mg/L). No other organic dyes, apart from the deliberately introduced Basic Red 9, were observed within the detection limits of the applied analytical methods. When the experiments were conducted under the previously optimized conditions, MSC600 achieved an adsorption capacity of 380.27 mg/g in the real wastewater, whereas MSC800 reached 272.54 mg/g. These values are modestly lower than those obtained in distilled water at the

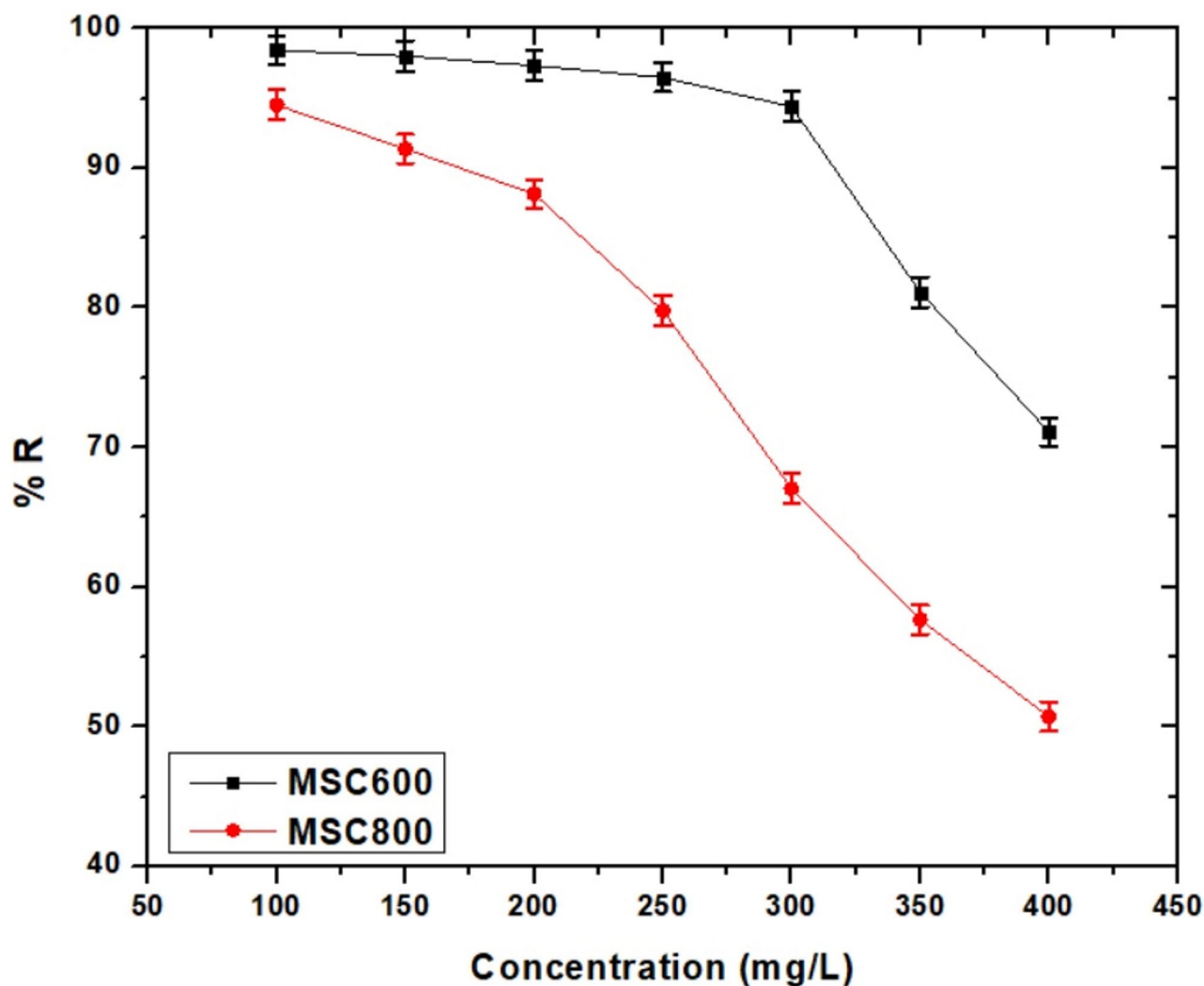


Fig. 15. Effect of initial basic red 9 concentration on removal of dye by MSC600 and MSC800 nano hybrids.

same initial dye concentration (436.68 mg/g for MSC600 and 313.48 mg/g for MSC800). The slight reduction in uptake is reasonably explained by competition between basic red 9 and the coexisting inorganic ions, along with potential site obstruction caused by dissolved constituents in the effluent. Despite this matrix effect, both adsorbents preserved strong removal performance, with MSC600 consistently outperforming MSC800. This trend supports the conclusion that the material possessing the larger specific surface area and more developed porosity maintains superior adsorption behavior even in complex wastewater systems, highlighting the promise of these nanocomposites for treating student laboratory effluents contaminated with basic red 9.

Conclusions

This work showed that $\text{Sr}_6\text{Co}_5\text{O}_{14.3}/\text{SrCO}_3/\text{MgO}/\text{C}$ and $\text{SrCoO}_{2.5}/\text{SrCO}_3/\text{MgO}/\text{Sr}(\text{OH})_2\cdot\text{H}_2\text{O}/\text{C}$ nano hybrids can be synthesized successfully by the Pechini sol-gel route at 600 and 800 °C. Structural and microscopic characterization confirmed multiphase ceramic metal oxides coupled with a carbon fraction and revealed clear differences in crystallite size and morphology between MSC600 and MSC800. Adsorption studies demonstrated very high capacities for basic red 9 with MSC600 and MSC800 reaching Langmuir maximum values of 436.68 and 313.48 mg, respectively. Kinetic and thermodynamic analyses indicated that dye uptake is fast, physical, exothermic, and spontaneous and follows the pseudo-first-order model and the Langmuir isotherm. Regeneration experiments and tests in real wastewater verified good reusability and robustness against coexisting ions, which highlights these nano hybrids as promising adsorbents for application in treating dye-containing effluents with basic red 9.

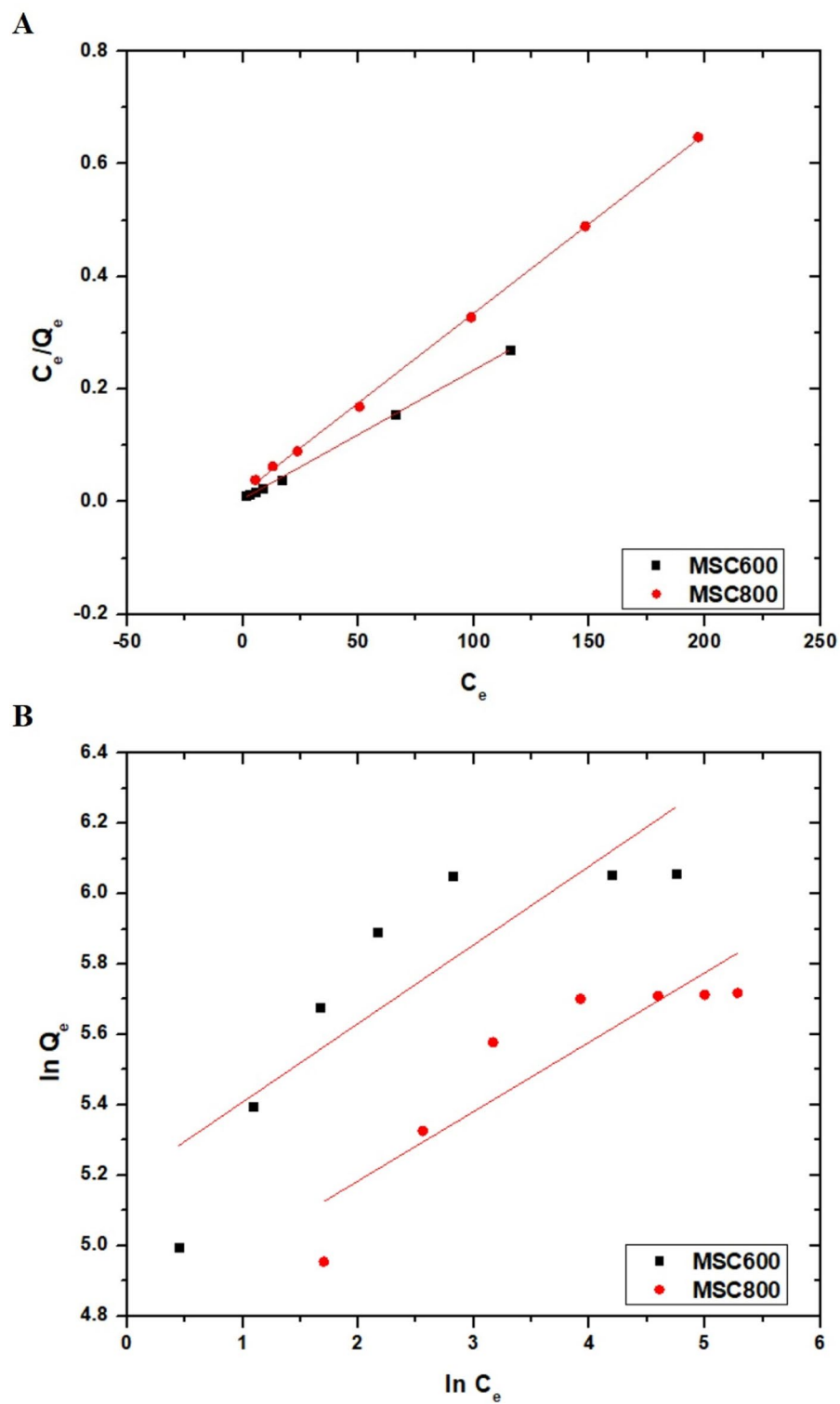


Fig. 16. (A) Langmuir and (B) Freundlich isotherms.

Nanohybrid	Langmuir			Freundlich			
	Q_{\max} (mg/g)	R^2	K_3 (L/mg)	K_4 (mg/g)(L/mg) ^{1/n}	Q_{\max} (mg/g)	1/n	R^2
MSC600	436.68	0.9995	0.4598	178.49	661.19	0.2235	0.7050
MSC800	313.48	0.9994	0.1961	120.24	381.87	0.1973	0.7794

Table 6. Langmuir and Freundlich constants for basic red 9 elimination employing MSC600 and MSC800 nanohybrids.

Adsorbent	Q_{\max} (mg/g)	Refs.
Activated carbon	69.82	⁵⁷
Lignocellulose	48.98	⁵⁸
Biochar	52.30	⁵⁹
Rice husk	7.20	⁶⁰
MSC600	436.68	This study
MSC800	313.48	This study

Table 7. Literature survey and comparison of Q_{\max} for basic red 9 elimination.

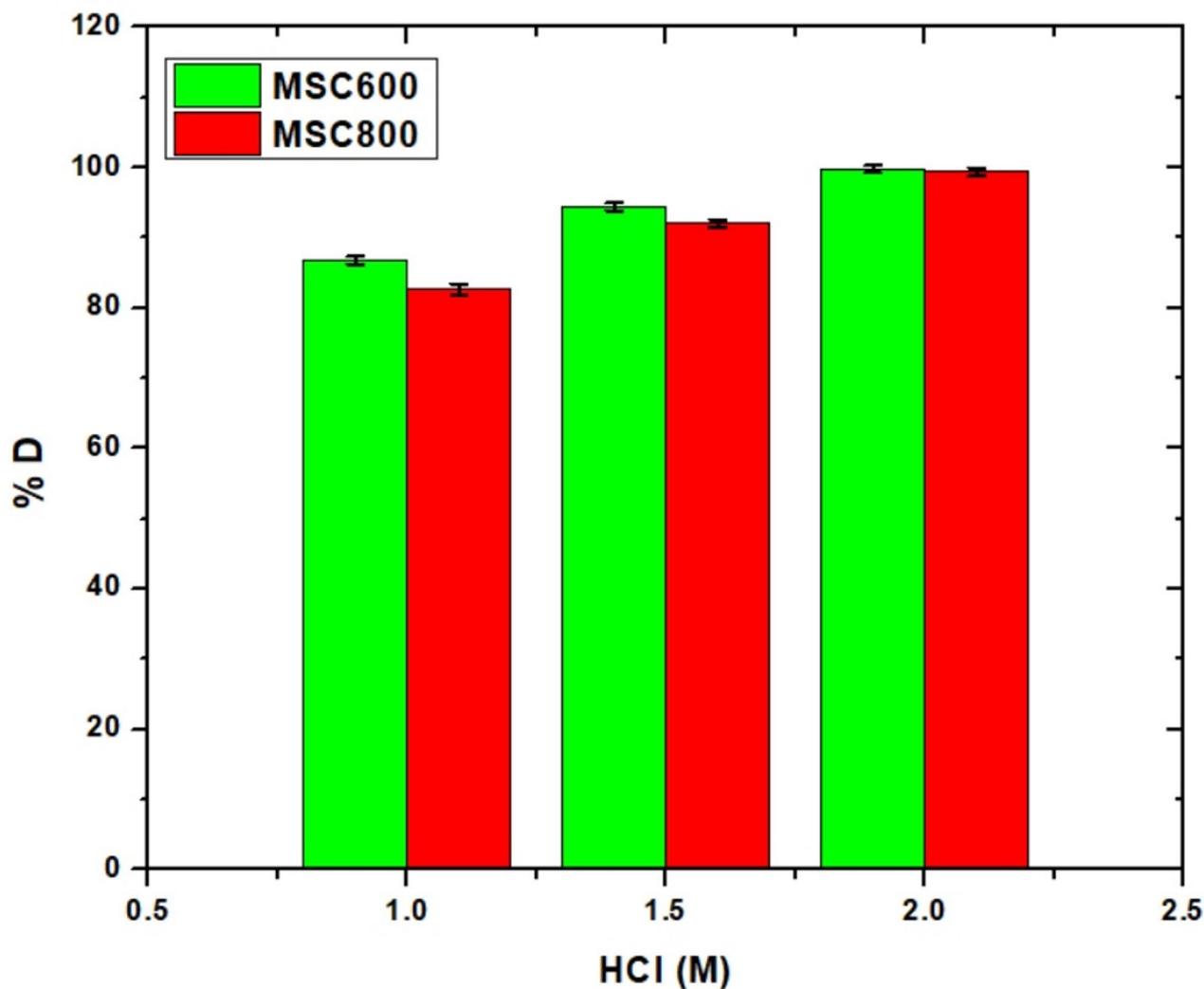


Fig. 17. Desorption efficiency of basic red 9 using HCl eluent for MSC600 and MSC800.

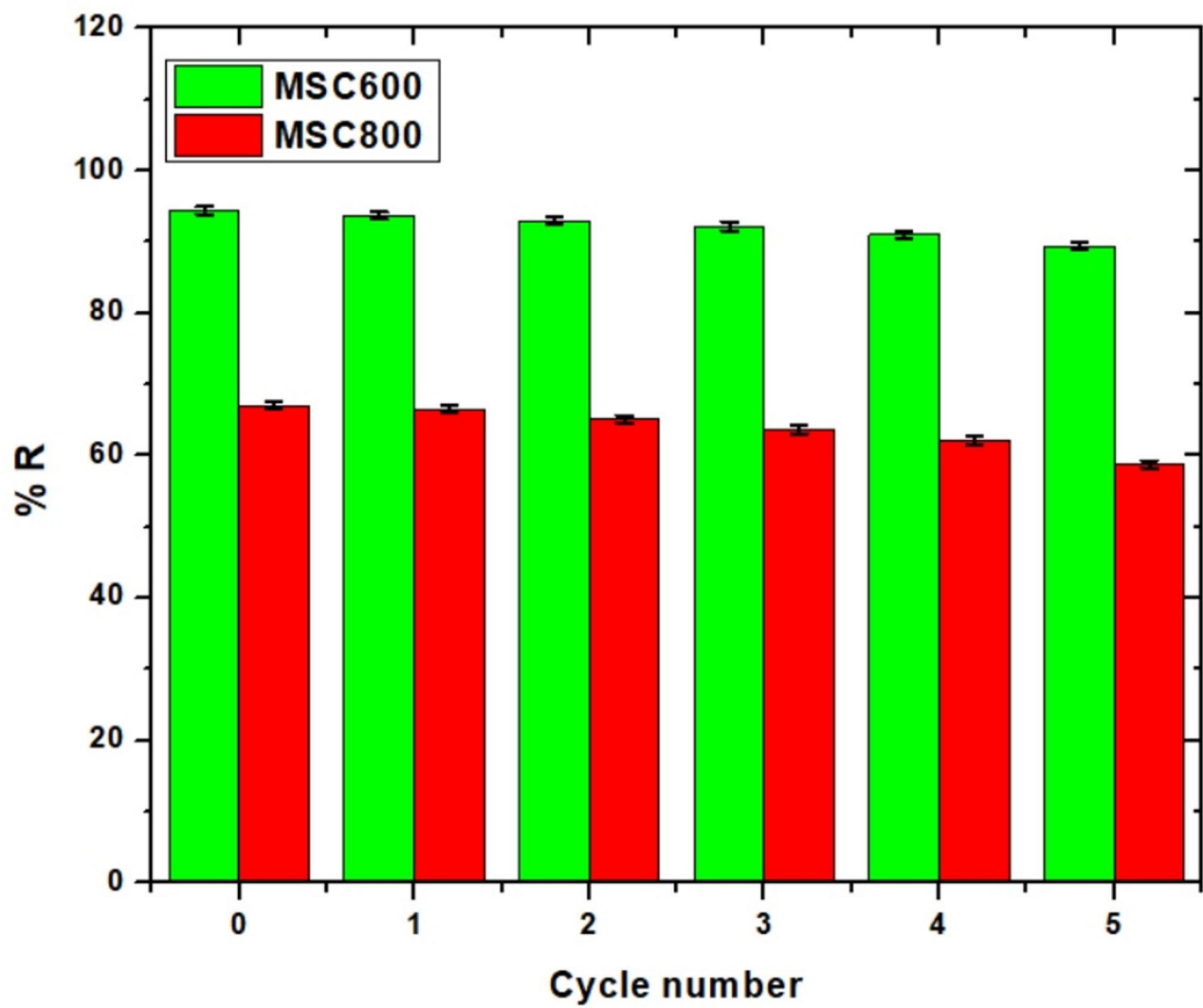


Fig. 18. Cyclic adsorption/desorption behavior of MSC600 and MSC800 over five consecutive runs.

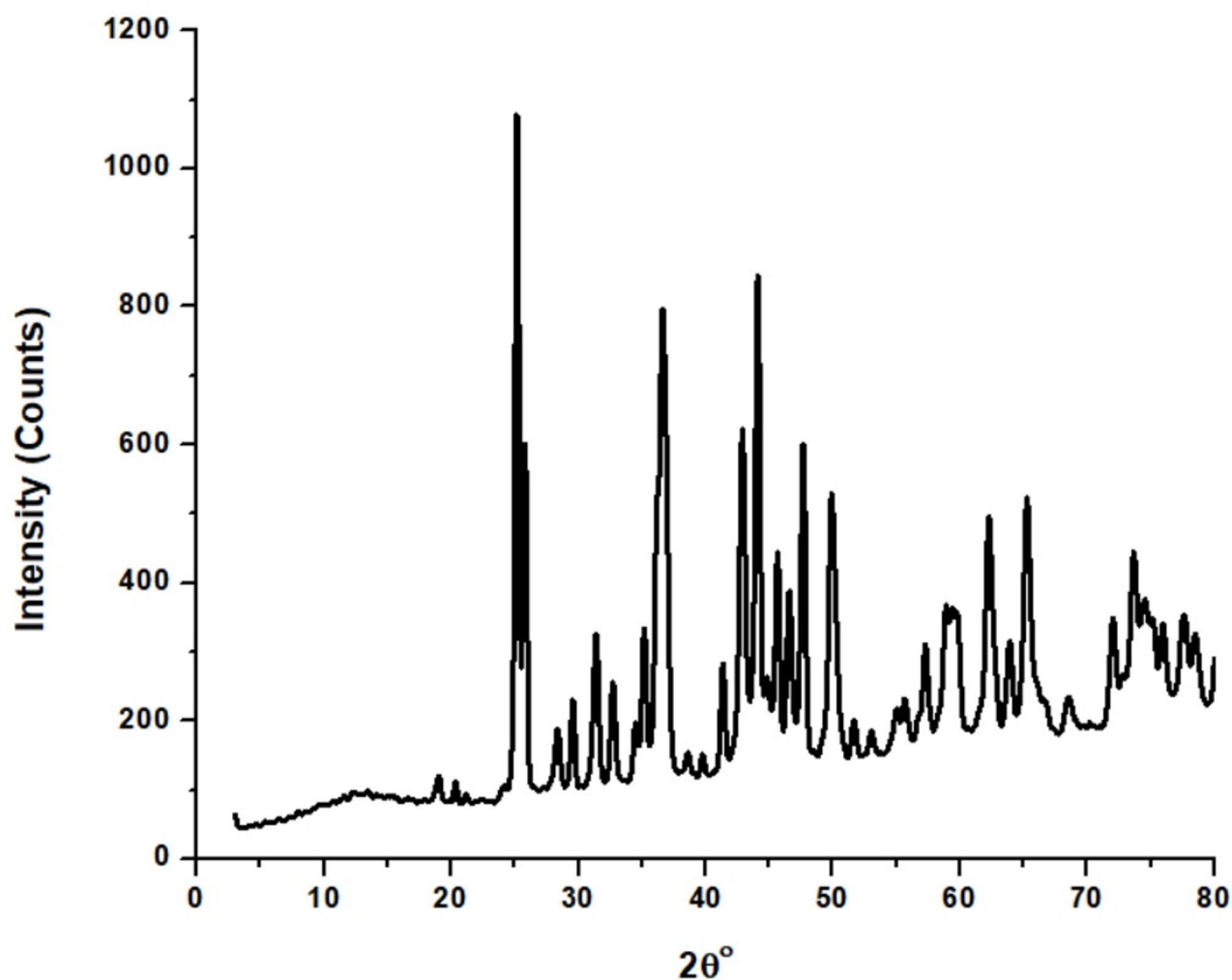


Fig. 19. XRD pattern of the regenerated MSC600 adsorbent after the fifth regeneration cycle.

Interfering ion	Q (mg/g) MSC600	Q (mg/g) MSC800	Reduction in Q (mg/g) MSC600	Reduction in Q (mg/g) MSC800
None (Control)	436.68	313.48	–	–
Na ⁺	431.25	309.76	5.43	3.72
K ⁺	427.43	306.92	9.25	6.56
Mg ²⁺	382.57	271.38	54.11	42.10
Ca ²⁺	369.84	259.64	66.84	53.84
Cl ⁻	433.19	310.57	3.49	2.91
NO ₃ ⁻	431.72	309.02	4.96	4.46
Methylene blue dye	305.36	213.57	131.32	99.91
Crystal violet dye	287.91	197.83	148.77	115.65

Table 8. Influence of interfering ions on elimination of basic red 9 dye employing MSC600 and MSC800 nano-hybrids.

Data availability

All data generated or analyzed in this study are included in the article.

Received: 10 January 2026; Accepted: 1 April 2026

Published online: 09 April 2026

References

- Silva, N. V. M., da Ladeira, A. C. Q. & Furtado, C. A. The use of carboxylated graphene oxides and related materials for the adsorption of metals and dyes: A review. *J. Mol. Liq.* **413**, 126001 (2024).
- Ahmed, M. J., Hameed, B. H., Anastopoulos, I. & Khanday, W. A. Recent advances in surfactant-functionalized materials as adsorbents for enhanced remediation of synthetic dyes: A review. *J. Taiwan. Inst. Chem. Eng.* **178**, 106398 (2026).
- Mnyango, J. I. et al. Sustainable wastewater treatment: Mechanistic, environmental, and economic insights into biochar for synthetic dye removal. *Next Mater.* **9**, 100974 (2025).
- Khamis, F., Hegab, H. M., Banat, F., Arafat, H. A. & Hasan, S. W. Comprehensive review on pH and temperature-responsive polymeric adsorbents: Mechanisms, equilibrium, kinetics, and thermodynamics of adsorption processes for heavy metals and organic dyes. *Chemosphere* **349**, 140801 (2024).
- Hevira, L., Ighalo, J. O. & Sondari, D. Chitosan-based polysaccharides for effective synthetic dye adsorption. *J. Mol. Liq.* **393**, 123604 (2024).
- Sağlam, S., Türk, F. N. & Arslanoğlu, H. Use and applications of metal-organic frameworks (MOF) in dye adsorption: Review. *J. Environ. Chem. Eng.* **11**, 110568 (2023).
- Mahajan, P., Jaspal, D. & Malviya, A. Adsorption of dyes using custard apple and wood apple waste: A review. *J. Indian Chem. Soc.* **100**, 100948 (2023).
- Rukaramato, R., Babatunde, D., Madanhire, T., Mketi, N. & Magwa, N. Nanocellulose-based materials for the removal of metal ions, pharmaceuticals, pesticides, dyes, and other pollutants from aqueous environments: A review. *J. Ind. Eng. Chem.* **150**, 265–299 (2025).
- Li, Y. et al. Efficient dye removal and antibacterial activity of imidazole-crosslinked chitosan hydrogel for wastewater treatment. *Int. J. Biol. Macromol.* **309**, 142904 (2025).
- Shi, Y. et al. A review on selective dye adsorption by different mechanisms. *J. Environ. Chem. Eng.* **10**, 108639 (2022).
- Silina, A., El Achari, A. & Salaün, F. Metal-organic framework electrospun nanofibers in application to dye removal from textile wastewaters: A review. *J. Environ. Chem. Eng.* **12**, 114819 (2024).
- Du, X. et al. Revisiting the efficacy of COF treatment for dyes in wastewater: A comprehensive review. *J. Environ. Chem. Eng.* **13**, 115660 (2025).
- Duman, O., Tunç, S. & Gürkan Polat, T. Adsorptive removal of triarylmethane dye (Basic Red 9) from aqueous solution by sepiolite as effective and low-cost adsorbent. *Microporous Mesoporous Mater.* **210**, 176–184 (2015).
- Fadeeva, N. P. et al. Development of composite ultrafiltration membrane from fly ash microspheres and alumina nanofibers for efficient dye removal from aqueous solutions. *Ceram. Int.* **50**, 52890–52903 (2024).
- Rakcho, Y. et al. Fabrication of low-cost ceramic nanofiltration membrane from natural resources for the removal of cationic and anionic dyes: Experimental and DFT investigations. *Chem. Eng. J.* **505**, 159779 (2025).
- Nataraj, S. K., Hosamani, K. M. & Aminabhavi, T. M. Nanofiltration and reverse osmosis thin film composite membrane module for the removal of dye and salts from the simulated mixtures. *Desalination* **249**, 12–17 (2009).
- Muniasamy, S. K., AlObaid, A. A., Warad, I. & Ravindiran, G. Removal of Brilliant Green dye in aqueous solution using synthetic coagulation and flocculation technique. *Desalin. Water Treat.* **314**, 231–240 (2023).
- Nnaji, P. C., Anadebe, V. C., Ezemagu, I. G. & Onukwuli, O. D. Potential of *Luffa cylindrica* seed as coagulation-flocculation (CF) agent for the treatment of dye wastewater: Kinetic, mass transfer, optimization and CF adsorption studies. *Arab. J. Chem.* **15**, 103629 (2022).
- Leng, Q. et al. Electrochemical removal of synthetic methyl orange dyeing wastewater by reverse electrodialysis reactor: Experiment and mineralizing model. *Environ. Res.* **214**, 114064 (2022).
- Shishir, M. K. H. et al. Photocatalytic removal of textile dyes: Analytical strategies for post-degradation evaluation. *Desalination* **617**, 119437 (2026).
- Zheng, X., Sun, J., Yang, M. & Li, Z. Facile construction of HOF@ZnO/TiO₂ ternary composite for efficient photocatalytic degradation of dyes. *Appl. Surf. Sci.* **718**, 164829 (2026).
- Periyasamy, A. P. A review of bioremediation of textile dye containing wastewater. *Clean. Water.* **4**, 100092 (2025).
- Mustafa, G. et al. Bioremediation of reactive blue 19 dye by laccase-producing *Serratia marcescens* AY4 strain. *J. Environ. Chem. Eng.* **13**, 115605 (2025).
- Abdulhameed, A. S., Omari, A., Younes, R. H., Algubri, S. & M. K. & Carboxylated chitosan-phthalate/ZrO₂ nanocomposite for removal of methylene blue dye: Characterization and adsorption modeling via response surface methodology. *J. Mol. Struct.* **1339**, 142386 (2025).
- Ayoob, H. W., Taieh, N. K., Abdullah, A. S., Homod, R. Z. & Medina, F. Salt effect and comparative analysis of micro and nano-bentonite in blue dye removal: Surface morphology and adsorption efficiency. *Powder Technol.* **468**, 121666 (2026).
- Ahmad, M. et al. DFT and comparative adsorption study of NiO, MnO, and Mn₂NiO₄ nanomaterials for the removal of amaranth dye from synthetic water. *RSC Adv.* **14**, 28285–28297 (2024).
- Mahmoud, H. R., Ibrahim, S. M. & El-Molla, S. A. Textile dye removal from aqueous solutions using cheap MgO nanomaterials: Adsorption kinetics, isotherm studies and thermodynamics. *Adv. Powder Technol.* **27**, 223–231 (2016).
- Kishore, K. et al. Efficient removal of toxic dyes from water using Mn₃O₄ nanoparticles: Synthesis, characterization, and adsorption mechanisms. *J. Mol. Struct.* **1333**, 141756 (2025).
- Ahmed, E. Nanocomposite for the immobilization or degradation of pollutants. *United States Patent Trademark Office.* **US12453951B**, 1 (2025).
- Ahmed, E. A. K. M. A. A. Nanocomposite for the immobilization or degradation of pollutants. *United States Patent Trademark Office.* **US12453952B**, 1 (2025).
- Hashemian, S., Rahimi, M. & Kerdegari, A. A. CuFe₂O₄@graphene nanocomposite as a sorbent for removal of alizarine yellow azo dye from aqueous solutions. *Desalin. Water Treat.* **57**, 14696–14707 (2016).
- Katowah, D. F. & Al-zahrani, H. K. A new ternary nanocomposites-based cellulose derivatives-CuFe₂O₄-zeolite with ultra-high adsorption capacity for Brilliant Green dye treatment and removal from the aquatic environment. *J. Saudi Chem. Soc.* **27**, 101764 (2023).
- Baroah, P., Mushahary, N., Das, B. & Basumatary, S. Waste biomass-based graphene oxide decorated with ternary metal oxide (MnO-NiO-ZnO) composite for adsorption of methylene blue dye. *Clean. Water.* **2**, 100049 (2024).
- Rajni et al. Revolutionizing wastewater treatment: Polymeric metal oxide nanocomposites for effective dye and heavy metal removal. *Chem. Eng. J.* **511**, 161694 (2025).
- Ahmed, E. Geopolymer composite for water decontamination. *United States Patent Trademark Office.* **US12274996B**, 1 (2025).
- Ahmed, E. Method of producing a mesoporous chitosan/NaFeSi₂O₆ based nanocomposite. *United States Patent Trademark Office.* **US12330137B**, 1 (2025).
- Rubab, R., Ali, S., Rehman, A. U., Khan, S. A. & Khan, A. M. Templated synthesis of NiO/SiO₂ nanocomposite for dye removal applications: Adsorption kinetics and thermodynamic properties. *Colloids Surf. Physicochem Eng. Asp.* **615**, 126253 (2021).
- Wang, M., Jiao, Y., Li, N. & Su, Y. Synthesis of a SiO₂-MgO composite material derived from yellow phosphorus slag with excellent malachite green adsorption activity. *J. Alloys Compd.* **969**, 172344 (2023).
- Saini, J., Garg, V. K. & Gupta, R. K. Removal of Methylene Blue from aqueous solution by Fe₃O₄@Ag/SiO₂ nanospheres: Synthesis, characterization and adsorption performance. *J. Mol. Liq.* **250**, 413–422 (2018).

40. Shaba, E. Y., Tijani, J. O., Jacob, J. O., Suleiman, M. A. T. & Mathew, J. T. Preparation, characterization, adsorptive and antimicrobial properties of Fe₃O₄@SiO₂@ZnO nanocomposite. *Colloids Surf. Physicochem Eng. Asp.* **686**, 133190 (2024).
41. Zhou, M. et al. Chelating adsorption-engaged anionic dye removal and Fenton-driven regeneration in ferromagnetic Ti/Co-LaFeO₃ perovskite. *Chem. Eng. J.* **479**, 147600 (2024).
42. Ahmed, E. *Synthesis of cobalt oxide nanoparticles using L-valine as a fuel* Vol. 12325643, 1 (United States Patent and Trademark Office, 2025).
43. Ahmed, E. Nanocomposite for wastewater treatment. *United States Patent Trademark Office.* **US12459834B**, 1 (2025).
44. Ehsanizadeh, S. A. et al. Pechini sol-gel synthesis, characterization, and electrochemical evaluation of ternary NdCoO₃/Co₃O₄/GO nanocomposite as a potential hydrogen storage material. *Int. J. Hydrogen Energy.* **128**, 146–158 (2025).
45. Jamdar, M. et al. Synthesis of SmMnO₃/Sm₂O₃ nanocomposites as efficient photocatalysts for organic dye degradation by sol gel pechini method. *Results Eng.* **21**, 101650 (2024).
46. Ranjeh, M., Beshkar, F., Amiri, O., Salavati-Niasari, M. & Moayedi, H. Pechini sol-gel synthesis of Cu₂O/Li₃BO₃ and CuO/Li₃BO₃ nanocomposites for visible light-driven photocatalytic degradation of dye pollutant. *J. Alloys Compd.* **815**, 152451 (2020).
47. Del Toro, R., Hernández, P., Díaz, Y. & Brito, J. L. Synthesis of La_{0.8}Sr_{0.2}FeO₃ perovskites nanocrystals by Pechini sol-gel method. *Mater. Lett.* **107**, 231–234 (2013).
48. Ahmed, E. Method of forming zinc oxide/borate nanocomposite. *United States Patent Trademark Office.* **US12275651B**, 1 (2025).
49. Ahmed, E. Mesoporous nanocomposite. *United States Patent Trademark Office.* **US12281048B**, 1 (2025).
50. Ahmed, E. CuMg_{0.5}Mn_{1.5}O₄/CuO nanocomposite material and method of making. *United States Patent Trademark Office.* **US12350652B**, 1 (2025).
51. Ahmed, E. Particulate nanocomposite material. *United States Patent Trademark Office.* **US12421125B**, 1 (2025).
52. Ahmed, E. Fabrication of Ca₃Co₄O₉/MgO nanocomposite materials using pechini sol-gel method. *United States Patent Trademark Office.* **US12357962B**, 1 (2025).
53. Ahmed, E. *Co₃O₄/CuO/MgO and (Cu_{0.97}Co_{0.03})O/MgO/CoO Nanocomposites and method of pechini sol-gel fabricating* Vol. 12358810, 1 (United States Patent and Trademark Office, 2025).
54. Abdelrahman, E. A., Shah, R. K., Abou-Krishna, M. M., Saad, F. A. & Munshi, A. M. Facile Synthesis and Characterization of Novel Fe_{0.65}Mg_{0.35}Cr₂O₄@C Nanocomposite for Efficient Removal of Cd(II) Ions from Aqueous Media. *Inorganics (Basel).* **13**, 82 (2025).
55. Al-Wasidi, A. S., Abdelrahman, E. A., Shah, R. K., Abdelhakim, N. A. & Saad, F. A. Facile synthesis of novel nanocomposite composed of Co₃O₄, MgO, and Mg₃B₂O₆ for malachite green dye decontamination from aqueous media. *Sci. Rep.* **14**, 30570 (2024).
56. Al-Wasidi, A. S., El-Sayyad, G. S., Saad, F. A., Shah, R. K. & Abdelrahman, E. A. Efficient removal of basic yellow 28 dye from water using facilely synthesized ZnO and Mg₃B₂O₆ nanostructures. *Sci. Rep.* **14**, 26181 (2024).
57. Sivarajasekar, N. & Baskar, R. Adsorption of basic red 9 onto activated carbon derived from immature cotton seeds: isotherm studies and error analysis. *Desalin. Water Treat.* **52**, 7743–7765 (2014).
58. Vo, H. N. et al. Removal of pararosaniline hydrochloride (basic red 9) from aqueous system with lignocellulose fraction of sugarcane bagasse as adsorbent. *Ind. Crops Prod.* **188**, 115573 (2022).
59. Côrtes, L. N. et al. Biochars from animal wastes as alternative materials to treat colored effluents containing basic red 9. *J. Environ. Chem. Eng.* **7**, 103446 (2019).
60. Sukmana, H. et al. Comparative Study of Adsorption of Methylene Blue and Basic Red 9 Using Rice Husks of Different Origins. *Recycling* **8**, 74 (2023).
61. Mukherjee, A., Dhak, P., Mandal, D. & Dhak, D. Solvothermal synthesis of 3D rod-shaped Ti/Al/Cr nano-oxide for photodegradation of wastewater micropollutants under sunlight: a green way to achieve SDG:6. *Environ. Sci. Pollut. Res.* **31**, 56901–56916 (2023).
62. Mukherjee, A. & Dhak, D. Biorefinery waste-based nanocomposites for industrial effluents treatment using physicochemical techniques. In *Biorefinery of Industrial Effluents for a Sustainable Circular Economy* 235–254 (Elsevier, 2025). <https://doi.org/10.1016/B978-0-443-21801-9.00016-1>
63. Mukherjee, A., Goswami, N. & Dhak, D. Photocatalytic Remediation of Industrial Dye Waste Streams Using Biochar and Metal-Biochar Hybrids: A Critical Review. *Chem. Afr.* **6**, 609–628 (2023).
64. Mukherjee, A., Dhak, P., Hazra, V., Goswami, N. & Dhak, D. Synthesis of mesoporous Fe/Al/La trimetallic oxide for photodegradation of various water-soluble dyes: Kinetic, mechanistic, and pH studies. *Environ. Res.* **217**, 114862 (2023).
65. Al-Kadhi, N. S., Abdelrahman, E. A., Alamro, F. S., Saad, F. A. & Al-Raimi, D. S. Innovative nanocomposite comprising of ZrO₂, MnCO₃, and CdCO₃ for superior crystal violet dye adsorption: synthesis, characterization, and regeneration insights. *Sci. Rep.* **15**, 5525 (2025).
66. Al-Kadhi, N. S. et al. Synthesis of novel magnesium ferrite Schiff base chitosan nanocomposite for efficient removal of pb(II) ions from aqueous media. *Sci. Rep.* **15**, 4153 (2025).
67. dos Santos, J. A. P., Pires, N. R., Loiola, A. R. & do Nascimento, R. F. New insights into the removal of indigo blue dye from aqueous effluent using a low-cost adsorbent. *Colloids Surf. Physicochem Eng. Asp.* **711**, 136338 (2025).
68. Rind, I. K., Lanjwani, M. F., Sari, A., Tuzen, M. & Saleh, T. A. Adsorption of Sudan II dye onto fly ash/polyacrylic acid/melamine composite: Factorial design optimization, reusability performance and removal mechanism. *Nano-Structures Nano-Objects.* **39**, 101283 (2024).
69. Al-Wasidi, A. S., Abdelrahman, E. A., Rehman, K., ur, Saad, F. A. & Munshi, A. M. Efficient removal of crystal violet and acid red 88 dyes from aqueous environments using easily synthesized copper ferrite nanoparticles. *Sci. Rep.* **14**, 29599 (2024).
70. Al-Kadhi, N. S., Al-Senani, G. M., Saad, F. A., Munshi, A. M. & Abdelrahman, E. A. Modification of nickel ferrite nanoparticles by sodium docusate surfactant for superior crystal violet dye removal from aqueous solutions. *Sci. Rep.* **14**, 27973 (2024).
71. Abdelrahman, E. A., Saad, F. A., Abou-Krishna, M. M., Khedr, A. M. & Alqahtani, Z. Straightforward Synthesis and Characterization of Analcime@Nickel Orthosilicate Novel Nanocomposite for Efficient Removal of Rhodamine B Dye from Aqueous Media. *Inorganics (Basel).* **13**, 120 (2025).
72. Kenawy, I. M. M., El-Reash, A., Hassanien, Y. G., Alnagar, M. M., Mortada, W. I. & N. R. & Use of microwave irradiation for modification of mesoporous silica nanoparticles by thioglycolic acid for removal of cadmium and mercury. *Microporous Mesoporous Mater.* **258**, 217–227 (2018).
73. Abdelrahman, E. A. Efficient adsorption of basic fuchsin dye using thermally engineered novel smart nanocomposites. *Sci. Rep.* **15**, 26232 (2025).
74. Abdelrahman, E. A. Simple Fabrication of SrCrO₄/MgO-Derived Hybrid Nanocomposites for Effective Crystal Violet Dye Adsorption from Aqueous Solutions. *J. Inorg. Organomet. Polym. Mater.* **35**, 8963–8975 (2025).
75. Hashem, M. A. et al. Dye adsorption on fish scale biosorbent from tannery wastewater. *Next Sustain.* **6**, 100112 (2025).
76. Gupta, S., Prajapati, A., Kumar, A. & Acharya, S. Synthesis of silica aerogel and its application for removal of crystal violet dye by adsorption. *Watershed Ecol. Environ.* **5**, 241–254 (2023).
77. Abdelrahman, E. A., Alduaij, O. K. & Shah, R. K. Novel nanocomposites including oxide, carbonate, and hydroxide phases for efficient methylene blue dye adsorption. *J. Science: Adv. Mater. Devices.* **11**, 101135 (2026).
78. Hui, Y., Liu, R., Lan, J., Sun, T. & Xu, A. Recyclable chitosan adsorbent: Facile functionalization strategy, excellent removal capacity of dyes and adsorption mechanism. *Chemosphere* **359**, 142291 (2024).
79. Zavala-Flores, E., Flores-López, Z., Alonso-Núñez, L., Espinoza-Gómez, H. & G. & Removal and adsorption kinetics of methylene blue dye by pristine cotton husk bracts (*Gossypium hirsutum* L.) from agroindustrial waste. *Ind. Crops Prod.* **209**, 117947 (2024).

80. Rajesh, Y. et al. Synthesis, characterization and adsorption studies on activated carbon adsorbent synthesized from *Kigelia africana* for removal of acid blue 113 dye from synthetic solution. *Mater. Today Proc.* **111**, 69–77 (2024).
81. Dalmaz, A. & Sivrıkaya Özak, S. Methylene blue dye efficient removal using activated carbon developed from waste cigarette butts: Adsorption, thermodynamic and kinetics. *Fuel* **372**, 132151 (2024).
82. Ullah, B. et al. Synthesis, characterization and adsorption studies of hydroxy ethyl cellulose grafted polyacrylic acid hydrogels; using basic yellow-28 as model dye. *Desalin. Water Treat.* **318**, 100360 (2024).
83. Al-Abbad, E. A., Rehman, R. & Hussain, M. S. A sustainable and cost-effective approach for efficient removal of Direct Blue-14 azo dye from wastewater using North American Zeolite for developing countries. *Phys. Chem. Earth Parts A/B/C.* **138**, 103888 (2025).
84. Moatamed Sabzevar, A., Ahmadpour, A., Ghahramaninezhad, M. & Arami-Niya, A. Improving structural properties and adsorption performance of kraft lignin-based microspheres for anionic dye removal. *Ind. Crops Prod.* **234**, 121640 (2025).
85. Rahmatpour, A., Alijani, N. & Alizadeh, A. H. Preparation of chitosan-based ternary nanocomposite hydrogel film by loading graphene oxide nanosheets as adsorbent for enhanced methylene blue dye removal. *Int. J. Biol. Macromol.* **253**, 126585 (2023).
86. Praipipat, P. et al. Synthesis and characterization of metal oxide doped beaded sugarcane bagasse fly ash for direct red 28 dye removal. *J. Ind. Eng. Chem.* **128**, 495–514 (2023).
87. Al-Wasidi, A. S. & Abdelrahman, E. A. Efficient remediation of malachite green dye utilizing novel and straightforwardly constructed nanocomposite. *J. Indian Chem. Soc.* **102**, 101994 (2025).

Acknowledgements

Princess Nourah bint Abdulrahman University Researchers Supporting Project number (PNURSP2026R85), Princess Nourah bint Abdulrahman University, Riyadh, Saudi Arabia.

Author contributions

Nada S. Al-Kadhi (Writing – Review & Editing), Saad A. Aljlil (Writing – Review & Editing), Maram T. Basha (Methodology, Investigation); Ehab A. Abdelrahman (Methodology, Conceptualization, Writing – Review & Editing).

Funding

Princess Nourah bint Abdulrahman University Researchers Supporting Project number (PNURSP2026R85), Princess Nourah bint Abdulrahman University, Riyadh, Saudi Arabia.

Declarations

Competing interests

The authors declare no competing interests.

Additional information

Correspondence and requests for materials should be addressed to E.A.A.

Reprints and permissions information is available at www.nature.com/reprints.

Publisher's note Springer Nature remains neutral with regard to jurisdictional claims in published maps and institutional affiliations.

Open Access This article is licensed under a Creative Commons Attribution-NonCommercial-NoDerivatives 4.0 International License, which permits any non-commercial use, sharing, distribution and reproduction in any medium or format, as long as you give appropriate credit to the original author(s) and the source, provide a link to the Creative Commons licence, and indicate if you modified the licensed material. You do not have permission under this licence to share adapted material derived from this article or parts of it. The images or other third party material in this article are included in the article's Creative Commons licence, unless indicated otherwise in a credit line to the material. If material is not included in the article's Creative Commons licence and your intended use is not permitted by statutory regulation or exceeds the permitted use, you will need to obtain permission directly from the copyright holder. To view a copy of this licence, visit <http://creativecommons.org/licenses/by-nc-nd/4.0/>.

© The Author(s) 2026